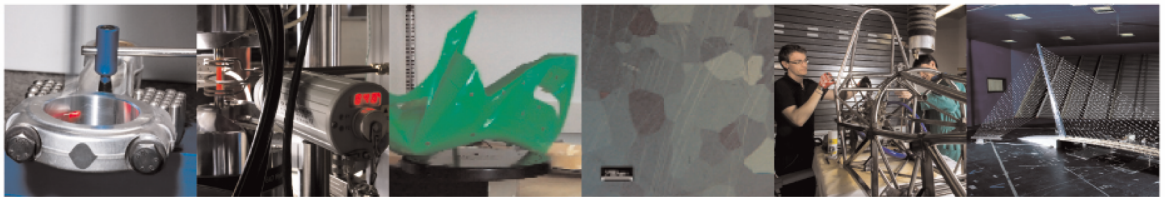# POLITECNICO
MILANO 1863

DIPARTIMENTO DI MECCANICA

mecc

A Nonlinear Reduced Order Model with Parametrized Shape Defects

Jacopo Marconi, Paolo Tiso, Francesco Braghin

A Nonlinear Reduced Order Model with Parametrized Shape Defects

Jacopo Marconi[a], Paolo Tiso[b,*], Francesco Braghin[a]

[a]*Department of Mechanical Engineering, Politecnico di Milano, Via La Masa 1, 20156 Milan, Italy*
[b]*Institute for Mechanical Systems, ETH Zürich, Leonhardstraße 21, 8092 Zürich, Switzerland*

Abstract

We propose a formulation to derive a reduced order model for geometric nonlinearities which is shown to be valid for a set of parametrized defects. The latter are imposed in terms of the superposition of precomputed perturbations of the nominal structure's 3D-mesh, and parametrized by their amplitudes. A reduced order model is then built *once and for all* using these defect shapes and the *nominal model* information only. A suitable reduced order basis is introduced as well in order to effectively represent the influence of the defects on the dynamics of the structure. In contrast to many nonlinear parametric reduced order models, the one we propose does not need any previous training of the model in the parameter space. In this way, prohibitively expensive full order simulations can be avoided and offline times are greatly reduced. Numerical tests are performed on a MEMS resonator and a silicon micro-beam to study the effect of shape imperfections on the dynamic response of the system.

Keywords: nonlinear modeling, reduced order models, continuum elements, parametric, geometric nonlinearities, defects

1. Introduction

The Finite Elements Method (FEM) is arguably one of the most popular analysis tool in a wide range of scientific and engineering fields. Nowadays many commercial software offer increasingly elaborate simulation packages which may even include multi-physics. Such programs usually come along with powerful Computer-Aided Design (CAD) environments which allow the representation of very complex systems, a crucial requirement in many disciplines. In mechanical engineering, very large FE models, counting several hundred thousands or even millions of degrees of freedom (dofs), are not rare. This fact leads to the necessity of Reduced Order Models (ROM) as a mean to alleviate computational burden and times.

Reduced Basis methods represent perhaps the most well-know and widespread way to come up with such ROMs. Loosely speaking, these approaches consist in selecting a suitable and reasonably small collection of vectors (the reduced basis) to approximate the full solution of the problem, of dimension N, with a M-dimensional reduced solution, where M is the number of basis vectors and M≪N. From this point onward, to

---

*Corresponding author
Email address:* `ptiso@ethz.ch` (Paolo Tiso)

compute a ROM one could follow a number of techniques, which largely depend on the availability of data (e.g. results coming from previous simulations), on the accessibility to the (FE) model and solvers, on the specific problem under study and on the physics involved (e.g. mechanics, fluid dynamics, thermal analysis).

Historically, in structural mechanics, *modal analysis* [1] has always been the most popular reduction method for linear dynamic simulations, where Galerkin projection is used to reduce the high dimensional space of the full structural model (often referred to as High Fidelity Model, HFM) to a low-dimensional space spanned by the Vibration Modes (VMs, i.e. the eigenvectors of the linear system, also known as natural modes) included in the projection basis. Substructuring techniques are also widely exploited, where the model is divided in multiple subsystem which can be independently reduced to be later assembled back together [2, 3, 4, 5].

In the context of nonlinear dynamics, the problem of running large FE models is way more severe than in a linear environment. However, even if resorting to model order reduction is almost mandatory, rigorous tools to do so are still object of research today. For this reason, in last years a huge effort has been made to develop nonlinear ROMs for a number of applications, ranging from contacts [6, 7], gears [8], bolted junctions [9] and flexible multi-body dynamics [10, 11] to geometric nonlinearities [12]. The latter topic will be the focus of this work. In spite of the fact that no unique or widely accepted technique has been established over the others, literature is mature enough to offer the analyst an ample range of choices to cope with the main challenges of model order reduction, namely, the selection of a Reduced Order Basis (ROB) and of an efficient way to compute reduced nonlinear generalized forces. With reference to the latter problem, three main options are available. A first way to proceed is to directly compute all the (modal) coupling stiffness coefficients (quadratic and cubic terms), task that can be accomplished through *non-intrusive* methods (i.e. not relying on low-level FE formulations, e.g. ICE - *Implicit Condensation and Expansion* method, where coefficients are identified from a set of static analyzes [13]) or through *intrusive* methods (i.e. where FE formulation must be available for manipulation [14]). Either ways, internal forces assume a polynomial form and can be directly evaluated, so that assembly of internal forces and tangent stiffness matrix is no longer required. A second option would be to resort to the so called *hyper-reduction* techniques, where the full internal force vector is obtained by computing forces on an extremely small set of elements only. This usually comes to the expense of relevant offline times, as the full solution is required to obtain the *training vectors* needed to identify the aforementioned set of elements. In a recent work [15], a method has been proposed to alleviate this problem by substituting this full nonlinear solution with a linear one, while in [16] an adaptive *a priori* approach is described. Last but not least, in the case of linear elastic material constitutive law, one may recognize that explicitly writing internal forces in terms of displacements leads to a third order polynomial, whose coefficients can be pre-computed and stored in second, third and fourth order tensors. This (intrusive) *tensorial approach* is the one we will adopt in this work, and it is crucial for our method. As for the problem of the ROB selection, again, many choices are possible. An extension of the popular Rayleigh-Ritz approach is given in [17], while an extensive review of basis vectors can be found in [18], where *dual modes*, a careful

2

selection of VMs and Proper Orthogonal Decomposition (POD) are discussed. In [19], an ad hoc recipe is given to find a suitable VM basis in the case of a circular cylincrical shells, even in presence of moderate imperfections. Here, however, we will make use *Modal Derivatives* (MDs) [20, 21], since they feature a set of advantages which make them better fit to our purposes, as it will be detailed later in Section 4.

All of the methods discussed above usually refer to a model of a structure whose geometry is well defined without uncertainty, model that in the remainder we will address to as the *nominal model*. In some circumstances however, it may be relevant to assess how a structure behaves in presence of *shape defects*. This is the case for instance of MEMS devices, whose dynamic response is usually strongly affected by the presence of manufacturing defects [22, 23]. Stochastic analysis is therefore often required to assess performances, and a Monte Carlo approach, where simulations are repeated for each and every set of randomly generated parameters, is usually the way to go. In terms of FE, a shape defect can be modeled by changing the nominal geometry and remeshing, or directly applying a transformation to the nodal coordinates of the nominal mesh. After the new mesh is obtained, matrices can be built and simulations performed. This procedure, with its variants, is already expensive for linear FE analysis, and for nonlinear analysis is simply inconceivable.

Two possible strategies can be used to address this problem. The first would be to resort to the family of the so called *reanalysis techniques*, which basically consist in exploiting a full, known response of a nominal structure to compute an approximate solution for the same structure with some kind of modification in geometry, mechanical properties or applied loads. Combined Approximations (CA) and Virtual Distortion Method (VDM) are two popular methods out of many available in literature [24]. To the authors' knowledge however, though these methods usually address *material nonlinearity* both for statics and dynamics [25], when it comes to *geometric nonlinearities* they address static problems only [26, 27], usually by alleviating the computational effort during Newton-Raphson equilibrium iterations.

The second option is to resort to to *parametric ROMs* (PROM). Again, as for ROMs, theory is well developed for linear analysis. Moment-matching is a popular strategy, where basically the (n-th) derivatives of the system equations with respect to the parameters (n-th moments) between the full and reduced models are required to match [28, 29, 30]. An extensive survey of existing (projection-based) methods for parametric reduced order models is given in [31], covering the issues of a proper selection of the ROB (e.g. mode-matching, POD), of the very construction of the model (e.g. global and local bases, basis/subspace/model interpolation) and of a correct sampling of the parameter space.

Parametric model order reduction for nonlinear problems is instead a field still in constant evolution, but which already displays a wide number of solutions. Most of these methods are again ROB based. However, while in many circumstances one can construct a ROB for nonlinear non-parametric ROMs and/or linear parametric ROMs just by exploiting information about the model, nonlinear PROMs usually rely upon a number of HFM simulations (or experimental data, if available) for the construction of the reduced model itself [6, 31]. Due to the way they are obtained, these two groups of ROMs are sometimes referred to as model-driven (or data-free) and data-driven, respectively. Hybrid solution are also possible, of course.

3

Then, nonlinear PROMs are (mostly) data-driven methods. The first step usually consists in sampling the parameter space at some locations (selected randomly, via greedy search algorithm, Latin Hypercube, Smolyak sparse grid, to name a few). The HFM solutions corresponding to these set of parameters are computed in a second phase. Following, a ROB is obtained performing a POD. This latter indeed features some nice properties, such as optimality of the (spatial) reduction basis and error bound. One can then use the basis obtained in this way directly [6] or use interpolation approaches between the available (trained) full solutions and/or bases in the parameter space to compute a new response for a new (untrained) parameter. Interpolation approaches are also used to approximate the nonlinear reduced terms [32, 33, 34]. Interpolation on Grassman manifold via tangent spaces is another popular option [35, 36], and data-regression techniques are also available. In [37] for instance, the CUR method was expanded to handle parametric dependence by building multidimensional interpolation functions for car crash simulations. At multiple stages, however, this method requires the expert's judgment and a good knowledge of the system under study (this is however justified, if not even desirable, in an industrial context).

While in [38, 39] ROM were sought to describe *localized* defects, the present work aim is to develop a nonlinear ROM to represent *shape defects* "parametrically", though this word assumes here a slightly different meaning than in the context depicted above. Rather than having a parameter describing a property or a physical dimension of the structure (e.g. density, length, width), here the parameter will define the amplitude of a shape representing the defect. More precisely, the defect will be given by the *linear superposition of precomputed shapes*, whose amplitudes are regulated by a parameter vector. Such defect shapes can be of any kind, as long as compatible with the boundary conditions of the nominal geometry. The final ROM, in tensorial form, will then be a function of the parameter vector, and will be able to describe any (small enough) variation of the system from the nominal geometry. Thus, to study a different defected configuration, remeshing will not be required anymore, as the defects will be embedded in the ROM formulation itself. To obtain such a model, an alternative expression for strains is required. This formulation was used by Budianksy to investigate post-buckling behavior of imperfect structures in Koiter analysis [40, 41]. Basically, it relies on the treatment of defects as additional fictitious displacements. The technique proved successful in a number of other works, as for instance in deriving the natural frequencies of imperfect beams and shells [42, 43] or to develop a ROM for buckling in presence of imperfections [44].

To summarize, the model-driven method we propose aims to provide a fast and versatile tool to aid the design phase of structures subject to known shape defects. Even if many domain mappings are available in literature to parametrize a geometry (see for instance [45], where free form deformations (FFD) are used), these shape defects are introduced in the strain formulation in order to be able to treat them as they were displacements. With respect to most methods already available in literature, which rely upon the sampling of the parameter space through multiple and highly expensive full simulations, this PROM requires only the nominal geometry of the structure and a set of user-defined shapes representing the defects. Without the need for training, offline costs to compute the model are therefore heavily cut down, while online computations

are extremely fast thanks to the explicit (tensorial) expression of the nonlinear internal forces. Moreover, in contrast to data-based methods that usually are valid only for a particular loading case (unless the load itself is included as a parameter to train), the obtained ROM can be run for an arbitrary number of different load cases (within the frequency validity range). Of course, the aforementioned benefits come at the expenses of *intrusiveness* and with the restrictions of small defects and of geometrical nonlinearities, whereas data-driven solutions have wider applicability. Moreover, it should also be mentioned that the presented model does not exhaustively address all the problems that may arise in connection to the presence of defects. In particular, residual or locked-in stresses are not taken into account in the present formulation.

The work is organized as follows: *Section* 2 will describe the procedure by which the defects are introduced in the nominal model as *fictitious* displacements, leading to a new form of the internal forces, without the need of reconstructing the full model for the structure afflicted by the imperfections. In *Section* 3 the new internal forces are explicitly written in a tensorial fashion (and directly in reduced form), featuring additional terms which depend on the selected set of defect-shapes. *Section* 4 will discuss suitable ROBs for the model at hand and will introduce a new kind of reduction shapes, representing defect-sensitivities, to enrich the projection basis. Nomenclature and procedures for the following numerical studies are introduced in *Section* 5. In *Section* 6 the model is validated on a test structure, representing a MEMS resonator, over a range of selected relevant defects, while in *Section* 7 a shallow arch is presented as a second example. Finally, in *Section* 8 conclusions are drawn.

2. Modified strain formulation

As already introduced in the previous section, the method we present here relies on the same procedure adopted by Budiansky in [40]. Its core assumption is to think of the defects as fictitious displacements to impose to the *nominal structure* (i.e. without defects). Strains associated to these defects produce non-physical stresses that need to be removed. We will make use of Budiansky's notation to better illustrate the concept.

Suppose that, under loading, a structure displaces by u. Introducing the linear and quadratic functionals L_1 and L_2, the strain can be written as

$$\varepsilon(u) = L_1(u) + \frac{1}{2}L_2(u). \tag{2.1}$$

By considering a fictitious displacement d representing the defect, the total strain, as described earlier, is given by

$$\begin{aligned}\varepsilon_{total} \approx \varepsilon' = \varepsilon(u+d) - \varepsilon(d) &= L_1(u+d) + \frac{1}{2}L_2(u+d) - L_1(d) - \frac{1}{2}L_2(d) \\ &= L_1(u) + \frac{1}{2}L_2(u) + L_{11}(u,d),\end{aligned} \tag{2.2}$$

where L_{11} is a bilinear functional operator defined as $L_2(u+d) = L_2(u) + L_{11}(u,d) + L_2(d)$, and where $\varepsilon(d)$ is the strain due to defects only.

5

From Eq. (2.2) it can be seen how an additional bilinear term in the strain expression appeared, depending on the defect. Corresponding internal forces will arise as well, allowing the parametrization of the model, as it will be later shown in Section 3.

In the following, these arguments - until now reported only in general terms, are applied to the case of tri-dimensional continuum mechanics and finite element discretization.

2.1. Continuum formulation

Let us consider a material point of final coordinates $\mathbf{X} = \{X, Y, Z\}$ after deformation, defined as

$$\mathbf{X} = \mathbf{x} + \mathbf{u} + \mathbf{u}_{\mathrm{d}}, \tag{2.3}$$

being $\mathbf{x} = \{x, y, z\}$ the initial coordinates, $\mathbf{u} = \{u, v, w\}$ the "real" displacement vector and $\mathbf{u}_{\mathrm{d}} = \{u_d, v_d, w_d\}$ the vector of small fictitious displacements corresponding to the defect along the three directions. According to continuum mechanics [46], we can define a strain measure considering the stretching of a line element undergoing the displacement $\mathbf{u} + \mathbf{u}_{\mathrm{d}}$. Differentiating Eq. (2.3) we obtain

$$d\mathbf{X} = \frac{\partial \mathbf{X}}{\partial \mathbf{x}} d\mathbf{x} = \frac{\partial (\mathbf{x} + \mathbf{u} + \mathbf{u}_{\mathrm{d}})}{\partial \mathbf{x}} d\mathbf{x} = (\mathbf{I} + \mathbf{D} + \mathbf{D}_{\mathrm{d}}) d\mathbf{x} = (\mathbf{F} + \mathbf{D}_{\mathrm{d}}) d\mathbf{x}, \tag{2.4}$$

where $\mathbf{I}, \mathbf{D}, \mathbf{D}_{\mathrm{d}}, \mathbf{F} \in \mathbb{R}^{3 \times 3}$ are the identity matrix, the (real) displacement-derivative matrix, the fictitious displacement-derivative matrix and the deformation gradient respectively. The stretch then is given by

$$d\mathcal{S} = d\mathbf{X}^T d\mathbf{X} - d\mathbf{x}^T d\mathbf{x}. \tag{2.5}$$

In our case however, we have first to remove the stretch associated to the defect only. Defining

$$\mathbf{X}_{\mathrm{d}} = \mathbf{x} + \mathbf{u}_{\mathrm{d}}, \tag{2.6}$$

and differentiating

$$d\mathbf{X}_{\mathrm{d}} = \frac{\partial \mathbf{X}_{\mathrm{d}}}{\partial \mathbf{x}} d\mathbf{x} = \frac{\partial (\mathbf{x} + \mathbf{u}_{\mathrm{d}})}{\partial \mathbf{x}} d\mathbf{x} = (\mathbf{I} + \mathbf{D}_{\mathrm{d}}) d\mathbf{x}, \tag{2.7}$$

we can define the stretch due to the defects only as

$$d\mathcal{S}_{\mathrm{d}} = d\mathbf{X}_{\mathrm{d}}^T d\mathbf{X}_{\mathrm{d}} - d\mathbf{x}^T d\mathbf{x}, \tag{2.8}$$

so that the total stretch is obtained subtracting Eq. (2.8) from Eq. (2.5) as

$$d\mathcal{S}' = d\mathbf{X}^T d\mathbf{X} - d\mathbf{X}_{\mathrm{d}}^T d\mathbf{X}_{\mathrm{d}} = \underbrace{d\mathbf{x}^T (\mathbf{F}^T \mathbf{F} - \mathbf{I}) d\mathbf{x}}_{\text{nominal structure}} + \underbrace{d\mathbf{x}^T (\mathbf{D}_{\mathrm{d}}^T \mathbf{D} + \mathbf{D}^T \mathbf{D}_{\mathrm{d}}) d\mathbf{x}}_{\text{mixed terms due to defects}} = 2(d\mathbf{x}^T \mathbf{E}_2 d\mathbf{x}), \tag{2.9}$$

where the contributions coming from the nominal structure and from the defects have been highlighted and where $\mathbf{E}_2$ is a modified version of the Green-Lagrange strain (second order) tensor. In particular, we can write

$$\mathbf{E}_2 = \underbrace{\frac{1}{2}(\mathbf{D}^T + \mathbf{D})}_{\mathbf{E}_2^l} + \underbrace{\frac{1}{2}\mathbf{D}^T \mathbf{D}}_{\mathbf{E}_2^q} + \underbrace{\frac{1}{2}\mathbf{D}_{\mathrm{d}}^T \mathbf{D} + \frac{1}{2}\mathbf{D}^T \mathbf{D}_{\mathrm{d}}}_{\mathbf{E}_2^d}, \tag{2.10}$$

6

being $\mathbf{E}_2^{l,q,d}$ the linear, quadratic and (bilinear) defect-related strain tensors respectively. Notice how Eq. (2.10) has the same structure predicted by Eq. (2.2). Using Voigt notation[1], the strain components can be written as

$$
\mathbf{E}_1 = \mathbf{E}_1^l + \mathbf{E}_1^q + \mathbf{E}_1^d = \begin{Bmatrix} \varepsilon_{xx} \\ \varepsilon_{yy} \\ \varepsilon_{zz} \\ \gamma_{xy} \\ \gamma_{xz} \\ \gamma_{yz} \end{Bmatrix} = \begin{Bmatrix} u_x \\ v_y \\ w_z \\ u_y + v_x \\ u_z + w_x \\ v_z + w_y \end{Bmatrix} + \begin{Bmatrix} \frac{1}{2}(u_x^2 + v_x^2 + w_x^2) \\ \frac{1}{2}(u_y^2 + v_y^2 + w_y^2) \\ \frac{1}{2}(u_z^2 + v_z^2 + w_z^2) \\ u_x u_y + v_x v_y + w_x w_y \\ u_x u_z + v_x v_z + w_x w_z \\ u_y u_z + v_y v_z + w_y w_z \end{Bmatrix} +
$$

$$
+ \begin{Bmatrix} u_x u_{d,x} + v_x v_{d,x} + w_x w_{d,x} \\ u_y u_{d,y} + v_y v_{d,y} + w_y w_{d,y} \\ u_z u_{d,z} + v_z v_{d,z} + w_z w_{d,z} \\ (u_{d,x} u_y + u_x u_{d,y}) + (v_{d,x} v_y + v_x v_{d,y}) + (w_{d,x} w_y + w_x w_{d,y}) \\ (u_{d,x} u_z + u_x u_{d,z}) + (v_{d,x} v_z + v_x v_{d,z}) + (w_{d,x} w_z + w_x w_{d,z}) \\ (u_{d,y} u_z + u_y u_{d,z}) + (v_{d,y} v_z + v_y v_{d,z}) + (w_{d,y} w_z + w_y w_{d,z}) \end{Bmatrix}, \quad (2.11)
$$

where $u_\star = \partial u/\partial \star$ and $u_{d,\star} = \partial u_d/\partial \star$ (with $\star = x, y, z$) are the displacement derivatives *with respect to the nominal initial configuration* (similar definitions for $v_\star\ v_{d,\star}$ and $w_\star\ w_{d,\star}$ hold).

The virtual work of internal forces can be written as

$$
W_{int} = \int_{V_o} \mathbf{S}_1^T \delta \mathbf{E}_1 \mathrm{d}V_o = \int_{V_o} \mathbf{S}_2 : \delta \mathbf{E}_2 \mathrm{d}V_o, \quad (2.12)
$$

being $\mathbf{S}_1^T = \{\sigma_{xx}, \sigma_{yy}, \sigma_{zz}, \tau_{xy}, \tau_{xy}, \tau_{yz}\}$ the Piola-Kirchhoff stress vector and $\mathbf{S}_2$ the corresponding tensor, the symbol ":" denoting double contraction. The integration volume is denoted by V_o. The virtual strain change is:

$$
\delta \mathbf{E}_2 = \frac{1}{2}\mathbf{F}^T \delta \mathbf{D} + \frac{1}{2}\delta \mathbf{D}^T \mathbf{F} + \underbrace{\frac{1}{2}\delta \mathbf{D}^T \delta \mathbf{D}}_{h.o.t.} + \frac{1}{2}\mathbf{D}_{\mathrm{d}}^T \delta \mathbf{D} + \frac{1}{2}\delta \mathbf{D}^T \mathbf{D}_{\mathrm{d}}, \quad (2.13)
$$

where higher order terms can be neglected for infinitesimal virtual displacements and where $\delta \mathbf{D}_{\mathrm{d}} = \mathbf{0}$, being the defect given.

In principle, since we are operating in a Lagrangian environment and we are defining all quantities with respect to the nominal configuration, the external work should be modified through push-forward/pull-back operations, depending if one defines the forces in the nominal or in the deformed configurations, respectively. This way, the changes induced by the defects on locations, areas and/or volumes onto which the external forces are applied would be correctly addressed. In the present work though we assume that the change between the two configurations is small, and therefore these aspects are neglected.

---

[1]We will use subscript 1 to denote Voigt notation, 2 to denote second order tensors.

2.2. Finite Element Formulation

Let us consider now a structure discretized using 3D-continuum elements and having n nodes per element. We define the *displacement derivative vector* and the defect derivative vector as

$$\boldsymbol{\theta} \in \mathbb{R}^9 : \boldsymbol{\theta} = \{u_x \ u_y \ u_z \ v_x \ v_y \ v_z \ w_x \ w_y \ w_z\}^T = \mathbf{G}\mathbf{p}, \tag{2.14}$$

$$\boldsymbol{\theta}_d \in \mathbb{R}^9 : \boldsymbol{\theta}_d = \{u_{d,x} \ u_{d,y} \ u_{d,z} \ v_{d,x} \ v_{d,y} \ v_{d,z} \ w_{d,x} \ w_{d,y} \ w_{d,z}\}^T = \mathbf{G}\mathbf{d}, \tag{2.15}$$

respectively, where $\mathbf{p} \in \mathbb{R}^{3n}$ is the nodal displacement vector of one element, $\mathbf{d} \in \mathbb{R}^{3n}$ is the nodal defect-displacement vector, and $\mathbf{G}$ is a matrix collecting the shape function derivatives with respect to physical coordinates. Recalling Eq. (2.11), we can define the strain vector as

$$\mathbf{E}_1 = \mathbf{E}_1^l + \mathbf{E}_1^q + \mathbf{E}_1^d = \mathbf{H}\boldsymbol{\theta} + \frac{1}{2}\mathbf{A}(\boldsymbol{\theta})\boldsymbol{\theta} + \mathbf{A}(\boldsymbol{\theta})\boldsymbol{\theta}_d = \left(\mathbf{H} + \frac{1}{2}\mathbf{A}(\boldsymbol{\theta}) + \mathbf{A}(\boldsymbol{\theta}_d)\right)\boldsymbol{\theta}, \tag{2.16}$$

where

$$\mathbf{H} = \begin{bmatrix} 1 & 0 & 0 & 0 & 0 & 0 & 0 & 0 & 0 \\ 0 & 0 & 0 & 0 & 1 & 0 & 0 & 0 & 0 \\ 0 & 0 & 0 & 0 & 0 & 0 & 0 & 0 & 1 \\ 0 & 1 & 0 & 1 & 0 & 0 & 0 & 0 & 0 \\ 0 & 0 & 1 & 0 & 0 & 0 & 1 & 0 & 0 \\ 0 & 0 & 0 & 0 & 0 & 1 & 0 & 1 & 0 \end{bmatrix}, \quad \mathbf{A}(\boldsymbol{\theta}) = \begin{bmatrix} u_x & 0 & 0 & v_x & 0 & 0 & w_x & 0 & 0 \\ 0 & u_y & 0 & 0 & v_y & 0 & 0 & w_y & 0 \\ 0 & 0 & u_z & 0 & 0 & v_z & 0 & 0 & w_z \\ u_y & u_x & 0 & v_y & v_x & 0 & w_y & w_x & 0 \\ u_z & 0 & u_x & v_z & 0 & v_x & w_z & 0 & w_x \\ 0 & u_z & u_y & 0 & v_z & v_y & 0 & w_z & w_y \end{bmatrix}. \tag{2.17}$$

Notice that in Eq. (2.16) the property $\mathbf{A}(\boldsymbol{\theta})\boldsymbol{\theta}_d = \mathbf{A}(\boldsymbol{\theta}_d)\boldsymbol{\theta}$ was exploited. For more details, the reader is referred to literature [46].

From Eq. (2.16), virtual strain variation writes

$$\delta\mathbf{E}_1 = (\mathbf{H} + \mathbf{A}(\boldsymbol{\theta}) + \mathbf{A}(\boldsymbol{\theta}_d))\mathbf{G}\delta\mathbf{p} = \mathbf{B}\delta\mathbf{p}, \tag{2.18}$$

where $\mathbf{B}$ is the strain-displacement matrix and, again, $\delta\boldsymbol{\theta}_d = 0$. Recalling Eq. (2.12), the internal virtual work writes

$$W_{int} = \delta\mathbf{p}^T \int_{V_o} \mathbf{B}^T \mathbf{S}_1 dV_o = \delta\mathbf{p}^T \mathbf{f}_{int} \tag{2.19}$$

while the internal force vector is given by

$$\mathbf{f}_{int} = \int_{V_o} \mathbf{B}^T \mathbf{S}_1 dV_o = \int_{V_o} \mathbf{B}^T \mathbf{C}_1 \mathbf{E}_1 dV_o, \tag{2.20}$$

where Hook's law $\mathbf{S}_1 = \mathbf{C}_1 \mathbf{E}_1$ has been introduced, being $\mathbf{C}_1$ the elastic constitutive matrix. From here on, one can take again the variation of internal forces and write an expression for the tangent stiffness matrix, which will include some additional terms generated by the defect.

3. Tensorial approach

In this section we derive the (element-level) tensors required to explicitly write the internal forces (and consequently the tangent stiffness matrix). Following Eq. (2.20), writing each term explicitly yields

$$\mathbf{f}_{int} = \int_{V_o} \mathbf{G}^T \left(\mathbf{H} + \mathbf{A} + \mathbf{A}_d\right)^T \mathbf{C}_1 \left(\mathbf{H} + \frac{1}{2}\mathbf{A} + \mathbf{A}_d\right) \mathbf{p} \; dV_o, \tag{3.1}$$

where $\mathbf{A}_d = \mathbf{A}(\boldsymbol{\theta}_d)$. Equation (3.1) can be split into the following contributions

$$\mathbf{f}^{(n,1)} = \mathbf{G}^T(\mathbf{H}^T\mathbf{C}_1\mathbf{H})\mathbf{G}\mathbf{p} = {}_2\mathbf{K}\mathbf{p}, \tag{3.2a}$$

$$\mathbf{f}^{(n,2)} = \mathbf{G}^T \left(\frac{1}{2}\mathbf{H}^T\mathbf{C}_1\mathbf{A} + \mathbf{A}^T\mathbf{C}_1\mathbf{H}\right) \mathbf{G}\mathbf{p}, \tag{3.2b}$$

$$\mathbf{f}^{(n,3)} = \frac{1}{2}\mathbf{G}^T(\mathbf{A}^T\mathbf{C}_1\mathbf{A})\mathbf{G}\mathbf{p}, \tag{3.2c}$$

$$\mathbf{f}^{(d,2)} = \mathbf{G}^T(\mathbf{H}^T\mathbf{C}_1\mathbf{A}_d + \mathbf{A}_d^T\mathbf{C}_1\mathbf{H})\mathbf{G}\mathbf{p}, \tag{3.2d}$$

$$\mathbf{f}^{(d,3)} = \mathbf{G}^T \left(\mathbf{A}^T\mathbf{C}_1\mathbf{A}_d + \frac{1}{2}\mathbf{A}_d^T\mathbf{C}_1\mathbf{A}\right) \mathbf{G}\mathbf{p} + \mathbf{G}^T(\mathbf{A}_d^T\mathbf{C}_1\mathbf{A}_d)\mathbf{G}\mathbf{p}, \tag{3.2e}$$

where, for convenience, integration over volume is implicitly assumed and where the superscript $^{(\star,i)}$ denotes terms associated to the nominal structure only ($\star = n$) or to the structure with defects ($\star = d$) of order i in $\mathbf{p}$ and/or $\mathbf{d}$. The linear stiffness term is trivially given by ${}_2\mathbf{K}$.

It is at this point convenient to re-express matrix $\mathbf{A}$ ($\mathbf{A}_d$) as

$$\mathbf{A} = \mathbf{L} \cdot \boldsymbol{\theta} = \mathbf{L} \cdot (\mathbf{G}\mathbf{p}), \tag{3.3}$$

being $\mathbf{L} \in \mathbb{R}^{6 \times 9 \times 9}$ a constant localization matrix, whose expression is given in Table 1.

Remark 1 (*notation*). In the following, we'll adopt the notation described in [47], which is compatible with the Matlab *Tensor Toolbox* [48] used in this work. In short, the notation $\mathbf{A} \cdot \mathbf{B}$ will always denote the contraction of the last dimension of $\mathbf{A}$ over the first dimension of $\mathbf{B}$. Where this is not the case, it will be explicitly indicated as $\mathbf{A} \cdot_{ij} \mathbf{B}$, meaning contraction of $\mathbf{A}$'s i^{th} dimension over $\mathbf{B}$'s j^{th} dimension. For matrices with more than two dimensions, transpose operation will be explicitly denoted as well. For instance, $\mathbf{A}^{T(i \leftrightarrow j)}$ means that dimension i is switched with dimension j. When Einstein's notation is used, we assume summation over the (repeated) *lowercase* indexes, while *uppercase* indexes are not to be summed over (e.g. $C_{IJ} = A_{Ii}B_{iJ}$).

3.1. Quadratic terms

Being the expression of the linear terms of equation (3.1) trivial, we start here by directly considering the quadratic ones. Upon a closer inspection of Equations (3.2)b-d, an underlying common structure can be recognized. For this reason, it will be sufficient to study the term

$$\mathbf{G}^T(\mathbf{H}^T\mathbf{C}_1\mathbf{A})\mathbf{G}\mathbf{p} \quad \rightarrow \quad (G^T H^T C)_{Ii}(L_{ijk}G_{kl}p_l)G_{jm}p_m = f_I, \tag{3.4}$$

$$L_{111} = 1, \quad L_{421} = 1, \quad L_{531} = 1, \quad L_{412} = 1, \quad L_{222} = 1,; \quad L_{632} = 1, \quad L_{513} = 1, \quad L_{623} = 1, \quad L_{333} = 1$$

$$L_{144} = 1, \quad L_{454} = 1, \quad L_{564} = 1, \quad L_{445} = 1, \quad L_{255} = 1, \quad L_{665} = 1, \quad L_{546} = 1, \quad L_{656} = 1, \quad L_{366} = 1$$

$$L_{177} = 1, \quad L_{487} = 1, \quad L_{597} = 1, \quad L_{478} = 1, \quad L_{288} = 1, \quad L_{698} = 1, \quad L_{579} = 1, \quad L_{689} = 1, \quad L_{399} = 1$$

By defining the third-order tensor $_3\hat{\mathbf{K}}$ as[2]

$$_3\hat{K}_{Ilm} p_l p_m = f_I, \tag{3.5}$$

we get to

$$_3\hat{K}_{IJK} = (G^T H^T C)_{Ii} (L_{ijk} G_{kJ}) G_{jK}, \tag{3.6a}$$

$$_3\hat{\mathbf{K}} = (\mathbf{G}^T \mathbf{H}^T \mathbf{C}_1) \cdot (\mathbf{L} \cdot \mathbf{G}) \cdot_{21} \mathbf{G}. \tag{3.6b}$$

Notice that $_3\hat{K}_{ijk} = {}_3\hat{K}_{ikj}$. Finally, using $_3\hat{\mathbf{K}}$, we can define

$$_3\mathbf{K} = \frac{1}{2} {}_3\hat{\mathbf{K}} + {}_3\hat{\mathbf{K}}^{T(1\leftrightarrow3)}, \tag{3.7}$$

$$_{3d}\mathbf{K} = {}_3\hat{\mathbf{K}} + {}_3\hat{\mathbf{K}}^{T(1\leftrightarrow3)}. \tag{3.8}$$

Recalling Eqs (3.2)b-d, it can be easily shown that the following expression hold

$$\mathbf{f}^{(n,2)} = ({}_3\mathbf{K} \cdot \mathbf{p})\mathbf{p}, \tag{3.9a}$$

$$\mathbf{f}^{(d,2)} = ({}_{3d}\mathbf{K} \cdot \mathbf{p})\mathbf{d}. \tag{3.9b}$$

Notice that all the computations here have been done only considering the terms in $\mathbf{p}$, but we would have obtained the same results even by using $\mathbf{A}_d$ instead of $\mathbf{A}$ in Eq. (3.4).

3.2. Cubic terms

As previously done for quadratic terms, even for cubic forces a core term can be isolated:

$$f_I = {}_4\hat{K}_{Ilqr} p_l^{(I)} p_q^{(II)} p_r = G_{Ii}^T (L_{ijk} G_{kl} p_l^{(I)})^{T(1\leftrightarrow2)} C_{jm} (L_{mnp} G_{pq} p_q^{(II)}) G_{nr} p_r, \tag{3.10}$$

which defines:

$$_4\hat{K}_{IJKL} = G_{Ii}^T (L_{ijk} G_{kJ})^{T(1\leftrightarrow2)} C_{jm} (L_{mnp} G_{pK}) G_{nL}, \tag{3.11a}$$

$$_4\hat{\mathbf{K}} = \mathbf{G}^T (\mathbf{L} \cdot \mathbf{G})^{T(1\leftrightarrow2)} \cdot_{21} \mathbf{C}_1 \cdot (\mathbf{L} \cdot \mathbf{G}) \cdot_{21} \mathbf{G}. \tag{3.11b}$$

---

[2]To avoid confusion with indexes, subscripts denoting tensors' names will be put on the left side

Notice that, according to this definition, internal forces are obtained following the sequence of products $((_4\hat{\mathbf{K}} \cdot \mathbf{p}) \cdot \mathbf{p}^{(II)})\mathbf{p}^{(I)}$. Recalling Eqs. (3.2)c-e, opportunely choosing $\mathbf{p}^{(I/II)}$ as $\mathbf{p}$ or $\mathbf{d}$ as required and using $_4\hat{\mathbf{K}}$, the following fourth-order tensors are defined:

$$_4\mathbf{K} = \frac{1}{2}\,_4\hat{\mathbf{K}}, \tag{3.12}$$

$$_{4d}\mathbf{K} = \,_4\hat{\mathbf{K}}^{T(2\leftrightarrow3)} + \frac{1}{2}\,_4\hat{\mathbf{K}}, \tag{3.13}$$

$$_{4dd}\mathbf{K} = \,_4\hat{\mathbf{K}}. \tag{3.14}$$

Thus, as it can be easily verified, internal forces write

$$\mathbf{f}^{(n,3)} = ((_4\mathbf{K} \cdot \mathbf{p}) \cdot \mathbf{p})\mathbf{p}, \tag{3.15}$$

$$\mathbf{f}^{(d,3)} = ((_{4d}\mathbf{K} \cdot \mathbf{p}) \cdot \mathbf{p})\mathbf{d} + ((_{4dd}\mathbf{K} \cdot \mathbf{p}) \cdot \mathbf{d})\mathbf{d}. \tag{3.16}$$

Finally, notice again that the tensors obtained in this and in previous section are defined for a *single element*. In theory, these could be assembled as usual into the global stiffness tensors. However, this is impossible in practice due to memory limitations. For this reason, Galerkin projection is applied at element level during the assembly procedure so that the global reduced tensors are directly obtained.

3.3. Tensor reduction

As shown previously, the quadratic and cubic terms of the internal forces write

$$\mathbf{f}^{(2)} = \mathbf{f}^{(n,2)} + \mathbf{f}^{(d,2)} = (_3\mathbf{K} \cdot \mathbf{p})\mathbf{p} + (_{3d}\mathbf{K} \cdot \mathbf{p})\mathbf{d}, \tag{3.17a}$$

$$\mathbf{f}^{(3)} = \mathbf{f}^{(n,3)} + \mathbf{f}^{(d,3)} = ((_4\mathbf{K} \cdot \mathbf{p}) \cdot \mathbf{p})\mathbf{p} + ((_{4d}\mathbf{K} \cdot \mathbf{p}) \cdot \mathbf{p})\mathbf{d} + ((_{4dd}\mathbf{K} \cdot \mathbf{p}) \cdot \mathbf{d})\mathbf{d}. \tag{3.17b}$$

Assume now to have a suitable reduction basis $\mathbf{V}$ for $\mathbf{p}$ and assume $\mathbf{d}$ to be a linear combination of a number of predefined defect shapes, collected by columns in matrix $\mathbf{U}$. Then, we can write

$$\mathbf{p} \approx \mathbf{V}\boldsymbol{\eta}, \tag{3.18a}$$

$$\mathbf{d} = \mathbf{U}\boldsymbol{\xi}, \tag{3.18b}$$

where $\mathbf{V} \in \mathbb{R}^{n\times m}$, $\mathbf{U} \in \mathbb{R}^{n\times m_d}$, $\boldsymbol{\eta} \in \mathbb{R}^m$ is the reduced coordinates vector, and $\boldsymbol{\xi} \in \mathbb{R}^{m_d}$ is the vector of defect-shape amplitudes, being n, m, m_d the number of dofs, modes in the basis, and defect-shapes, respectively. Substituting equations (3.18) into (3.17), we can write the following reduced tensors, here written in tensor and Einstein notations:

$$
\begin{aligned}
&_3\mathbf{Q} = ((\mathbf{V}^T \cdot \,_3\mathbf{K}) \cdot \mathbf{V}) \cdot_{21} \mathbf{V} && _3Q_{IJK} = V_{Ii}^T \,_3K_{ijk} V_{kJ} V_{jK} \\
&_{3d}\mathbf{Q} = ((\mathbf{V}^T \cdot \,_{3d}\mathbf{K}) \cdot \mathbf{V}) \cdot_{21} \mathbf{U} && _{3d}Q_{IJK} = V_{Ii}^T \,_{3d}K_{ijk} V_{kJ} U_{jK} \\
&_4\mathbf{Q} = (((\mathbf{V}^T \cdot \,_4\mathbf{K}) \cdot \mathbf{V}) \cdot_{31} \mathbf{V}) \cdot_{21} \mathbf{V} \quad \Longleftrightarrow \quad && _4Q_{IJKL} = V_{Ii}^T \,_4K_{ijkl} V_{lJ} V_{kK} V_{jL} && (3.19) \\
&_{4d}\mathbf{Q} = (((\mathbf{V}^T \cdot \,_{4d}\mathbf{K}) \cdot \mathbf{V}) \cdot_{31} \mathbf{V}) \cdot_{21} \mathbf{U} && _{4d}Q_{IJKL} = V_{Ii}^T \,_{4d}K_{ijkl} V_{lJ} V_{kK} U_{jL} \\
&_{4dd}\mathbf{Q} = (((\mathbf{V}^T \cdot \,_{4dd}\mathbf{K}) \cdot \mathbf{V}) \cdot_{31} \mathbf{U}) \cdot_{21} \mathbf{U} && _{4dd}Q_{IJKL} = V_{Ii}^T \,_{4dd}K_{ijkl} V_{lJ} U_{kK} U_{jL}
\end{aligned}
$$

where $_3\mathbf{Q} \in \mathbb{R}^{m \times m \times m}$, $_{3d}\mathbf{Q} \in \mathbb{R}^{m \times m \times m_d}$, $_4\mathbf{Q} \in \mathbb{R}^{m \times m \times m \times m}$, $_{4d}\mathbf{Q} \in \mathbb{R}^{m \times m \times m \times m_d}$ and $_{4dd}\mathbf{Q} \in \mathbb{R}^{m \times m \times m_d \times m_d}$. The reduced internal force vectors for quadratic and cubic terms write

$$\tilde{\mathbf{f}}^{(2)} = (_3\mathbf{Q} \cdot \boldsymbol{\eta})\boldsymbol{\eta} + (_{3d}\mathbf{Q} \cdot \boldsymbol{\xi})\boldsymbol{\eta}, \tag{3.20a}$$

$$\tilde{\mathbf{f}}^{(3)} = ((_4\mathbf{Q} \cdot \boldsymbol{\eta}) \cdot \boldsymbol{\eta})\boldsymbol{\eta} + ((_{4d}\mathbf{Q} \cdot \boldsymbol{\xi}) \cdot \boldsymbol{\eta})\boldsymbol{\eta} + ((_{4dd}\mathbf{Q} \cdot \boldsymbol{\xi}) \cdot \boldsymbol{\xi})\boldsymbol{\eta}. \tag{3.20b}$$

Finally, notice that

    i. once $\mathbf{V}$ and $\mathbf{U}$ are selected and tensors from Eqs. (3.19) are computed, defects can be toggled on/off and leveraged just by changing $\boldsymbol{\xi}$, the parameter-vector of defect shapes amplitudes

    ii. the terms $(_{3d}\mathbf{Q} \cdot \boldsymbol{\xi})$, $((_{4dd}\mathbf{Q} \cdot \boldsymbol{\xi}) \cdot \boldsymbol{\xi})$ and $(_{4d}\mathbf{Q} \cdot \boldsymbol{\xi})$ can be precomputed before each analysis and added to $_2\mathbf{Q}$ and $_3\mathbf{Q}$, respectively; thus, online computations will involve only three tensors rather than five.

    iii. generally speaking, the formulae derived in this paragraph are valid either referred to the global structure or to the single element. As mentioned earlier though, projection should be carried out at element level (in which case one should use $\mathbf{V}^{el}$, the element-partition of $\mathbf{V}$).

    iv. the tensorial formulation arises from linear elastic constitutive law and Total Lagrangian formulation. Should other kinematic models (e.g. corotational) be adopted, the polynomial formulation should be retrieved (e.g. using Taylor expansion) before applying the presented method.

4. Enhanced basis for defects

To compute the reduced tensors, one needs to specify first (a) the defect-shapes in $\mathbf{U}$ and (b) the reduced order basis (ROB) $\mathbf{V}$. The choice of the latter is critical, since the most expensive step of the present method corresponds to the offline computation of the tensors which, as already highlighted, can only be obtained directly in reduced form. An *a priori* selection of the ROB is then crucial, as most (if not all) of the advantages provided by the present approach would be lost if one had to choose a new basis and compute the reduced tensors for every and each different choice of the parameter-vector $\boldsymbol{\xi}$.

As already mentioned in the introduction, the choice of a projection basis for a parametric model can be done as proposed by a number of different parametric model order reduction techniques (e.g. moment-matching, POD). However, the particular form of the internal forces (which follows from the strain formulation, Eq. (2.11)) allows for another option, that will be now discussed.

We first tested a ROB with vibration modes (VMs) and modal derivatives (MDs) in their static form [49], computed on the *nominal structure*. We here briefly recall how to compute MDs with reference to continuum elements. MDs are defined as

$$\boldsymbol{\theta}_{ij} \triangleq \frac{\partial \boldsymbol{\phi}_i}{\partial \eta_j} = -\mathbf{K}|_{eq}^{-1} \frac{\partial \mathbf{K}(\boldsymbol{\phi}_j \eta_j)}{\partial \eta_j}\bigg|_{eq} \boldsymbol{\phi}_i, \tag{4.1}$$

12

where ϕ_j is the j-th vibration mode, η_j its modal amplitude and $\mathbf{K}$ is the tangent stiffness matrix. The tangent stiffness matrix evaluated for a displacement $\mathbf{p} = \phi_j \eta_j$ writes (at element level):

$$\mathbf{K}^{el} = \frac{\partial \mathbf{f}^{el}}{\partial \mathbf{p}^{el}} = \int_{V_o} \mathbf{G}^T \left[\mathbf{H}^T \mathbf{C} \mathbf{H} + \mathbf{H}^T \mathbf{C} \mathbf{A}_\eta + 2 \mathbf{A}_\eta^T \mathbf{C} \mathbf{H} + 3 \mathbf{A}_\eta^T \mathbf{C} \mathbf{A}_\eta \right] \mathbf{G} \, dV_o, \tag{4.2}$$

where $\mathbf{A}_\eta = \mathbf{A}(\mathbf{G}\phi_j^{el}\eta_j)$. Taking the derivative with respect to the modal coordinate η_j and evaluating the resulting expression at equilibrium (i.e. for $\eta_j = 0$) leads to

$$\frac{\partial \mathbf{K}^{el}(\phi_j^{el}\eta_j)}{\partial \eta_j}\bigg|_{eq} = \int_{V_o} \mathbf{G}^T \left[\mathbf{H}^T \mathbf{C} \mathbf{A}_\phi + 2 \mathbf{A}_\phi^T \mathbf{C} \mathbf{H} \right] \mathbf{G} \, dV_o, \tag{4.3}$$

where $\mathbf{A}_\phi = \mathbf{A}(\mathbf{G}\phi_j^{el})$. This last equation defines the derivative of the tangent stiffness matrix with respect to the j-th modal coordinate *at element level*, and can be assembled for the whole system following the usual FE procedures; then Eq. (4.1) can be evaluated.

With VMs and MDs only, however, the basis proves to be sufficient to represent a subclass of defects only. In particular it yields accurate results only when the defect-base $\mathbf{U}$ corresponds to a subset of VMs. The reason why this happens is likely to reside in the fact that MDs are included in the ROB, and MDs represent *de facto* modal sensitivities.

On the stream of these considerations, the idea is then to enrich the ROB adding *defect sensitivities* (DSs). A similar approach was used in [50], where POD-modes sensitivities were added to the ROB to model the flow past a square cylinder, with the incidence angle as a geometric parameter. The method showed better accuracy with respect to other traditional POD-based approaches. DSs are obtained following the same procedure to compute MDs. Consider the eigenvalue problem evaluated at equilibrium (i.e. for $\mathbf{p} = \mathbf{0}$):

$$\left(\mathbf{K}|_{eq} - \omega_i^2 \mathbf{M} \right) \phi_i = 0, \tag{4.4}$$

being ω_i and $\phi_i \in \mathbb{R}^n$ the i-th eigenfrequency and eigenvector respectively. Moreover, recalling Eqs. (3.1), (3.2) and (3.17) the tangent stiffness matrix $\mathbf{K}$ writes

$$\mathbf{K}(\mathbf{p}, \mathbf{d}) = \frac{\partial \mathbf{f}_{int}}{\partial \mathbf{p}} = {}_2\mathbf{K} + 2{}_3\mathbf{K} \cdot \mathbf{p} + 3({}_4\mathbf{K} \cdot \mathbf{p}) \cdot \mathbf{p} + {}_{3d}\mathbf{K} \cdot_{21} \mathbf{d} + 2({}_{4d}\mathbf{K} \cdot \mathbf{p}) \cdot_{21} \mathbf{d} + ({}_{4dd}\mathbf{K} \cdot_{31} \mathbf{d}) \cdot_{21} \mathbf{d}, \tag{4.5}$$

and is thus a function of both displacements and defects. Taking the derivative of the eigenvalue problem with respect to the j-th amplitude parameter ξ_j and assuming $\xi_i = 0$ for $i \neq j$ (so that $\mathbf{d} = \mathbf{U}_j \xi_j$), we write

$$\left(\mathbf{K}|_{eq} - \omega_i^2|_{eq}\mathbf{M} \right) \frac{\partial \phi_i}{\partial \xi_j}\bigg|_{eq} + \left(\frac{\partial \mathbf{K}}{\partial \xi_j}\bigg|_{eq} - \frac{\partial \omega_i^2}{\partial \xi_j}\bigg|_{eq} \mathbf{M} \right) \phi_i|_{eq} = \mathbf{0}. \tag{4.6}$$

Notice that $\mathbf{M}$ is the mass matrix referred to the *nominal system*, and it is assumed not to vary significantly in presence of defects (its derivatives w.r.t. ξ_j are therefore zero). Equation (4.6) cannot directly be solved for $\partial \phi_i / \partial \xi_j$ since the coefficient matrix is singular by definition. Though workarounds can be found in literature, here we prefer to neglect mass terms as it's done for static MDs, allowing us to define DSs as

$$\boldsymbol{\Xi}_{ij} \triangleq \frac{\partial \phi_i}{\partial \xi_j}\bigg|_{eq} = -\mathbf{K}|_{eq}^{-1} \frac{\partial \mathbf{K}}{\partial \xi_j}\bigg|_{eq} \phi_i, \tag{4.7}$$

13

which represent the sensitivity of mode i with respect to defect j. In Eq. (4.7), $\mathbf{K} = \mathbf{K}(\mathbf{p}, \mathbf{d})$ must be evaluated for $\mathbf{p} = \mathbf{0}$ (equilibrium) and $\mathbf{d} = \mathbf{U}_j \xi_j$, as well as its derivative $\partial \mathbf{K}/\partial \xi_j$. Strictly speaking, however, we have that the latter depends on ξ_j. This is not desirable, as it would make the ROB $\mathbf{V}$ depend on the parameter amplitude. We can make then the further assumption to take the stiffness matrix derivative around the nominal configuration, that is for $\xi_j = 0$. This way we have, for the single element,

$$\left. \frac{\partial \mathbf{K}^{el}}{\partial \xi_j} \right|_{eq} = \frac{\partial \mathbf{K}^{el}(\mathbf{p}^{el} = \mathbf{0}, \mathbf{d} = \mathbf{U}_j^{el} \xi_j)}{\partial \xi_j} = \mathbf{G}^T \left(\mathbf{H}^T \mathbf{C}_1 \mathbf{A}_d + \mathbf{A}_d^T \mathbf{C}_1 \mathbf{H} + 2\xi_j \mathbf{A}_d^T \mathbf{C}_1 \mathbf{A}_d \right) \mathbf{G} \tag{4.8a}$$

$$= \mathbf{G}^T \left(\mathbf{H}^T \mathbf{C}_1 \mathbf{A}_d + \mathbf{A}_d^T \mathbf{C}_1 \mathbf{H} \right) \mathbf{G}, \tag{4.8b}$$

where $\mathbf{U}_j^{el}$ is the element subset of the j-th column of $\mathbf{U}$ and where, in this case, $\mathbf{A}_d = \mathbf{A}(\mathbf{G}\mathbf{U}_j^{el})$. Finally, $(\partial \mathbf{K}/\partial \xi_j)|_{eq}$ is formed through standard finite element assembly.

In conclusion, the ROB will be composed of a set of m VMs $\boldsymbol{\phi}_i$, collected in matrix $\boldsymbol{\Phi}$, a set of $m(m+1)/2$ (S)MDs $\boldsymbol{\theta}_{ij}$, collected in matrix $\boldsymbol{\Theta}$, and a set of $m_d m$ DSs $\boldsymbol{\Xi}_{ij}$, collected in matrix $\boldsymbol{\Upsilon}$, so that

$$\mathbf{V} = [\boldsymbol{\Phi}, \boldsymbol{\Theta}, \boldsymbol{\Upsilon}], \tag{4.9}$$

for a total of $(3/2 + m/2 + m_d)m$ basis vectors. As already mentioned, in the particular case in which defects are chosen from the set of VMs, and these VMs with associated MDs are included in the basis, then one could avoid to compute their respective DSs, reducing the size of the ROB. However, since rigorously $\boldsymbol{\theta}_{ij} \neq \boldsymbol{\Xi}_{ij}$, this would be just an approximation. Refer to Appendix A for more details.

Remark 2 (*on basis selection*). Generally speaking, not all the MDs and DSs in the projection basis will be strictly required to obtain an accurate ROM. Techniques to select a subset of MDs are already available in literature [49, 51] and one could think of applying similar strategies even to DSs. Though an interesting topic, as $\mathbf{V}$'s dimension strongly affects both offline and online computational times, this is out of the scope of the present work. Therefore, it will not be treated here.

5. Method

5.1. Model types

We test the proposed method on a FE model of a realistic system. For each selected combination of defects, simulations are performed for four different models. First, the solution is computed for the high fidelity model including defects (HFM-d) and its "classic" reduced counterpart (ROM-d), that is without the new strain definition and without parametrization. By this we mean that the reduced order basis $\mathbf{V}$ is obtained form the mesh that directly incorporates defects. As such, DDs are not needed. Secondly, the Defect-Parametric Reduced Order Model (DP-ROM) will be run. This refers to the ROM discussed in this work. Finally, the "classic" ROM-n computed from the high fidelity *nominal* model (HFM-n) is simulated

14

Table 2: Acronyms for the different models considered in the numerical study.

MODEL	Description
HFM-n	high fidelity model of the *nominal* structure (i.e. without defects)
HFM-d	high fidelity model of the structure *with defects*
ROM-n	"classic" reduced order model (with VMs and MDs) in tensorial form, computed from the HFM-n
ROM-d	"classic" reduced order model (with VMs and MDs) in tensorial form, computed from the HFM-d
DP-ROM	*defect-parametric* ROM (with VMs, MDs and DSs) in tensorial form, computed from HFM-n and a given set of defects
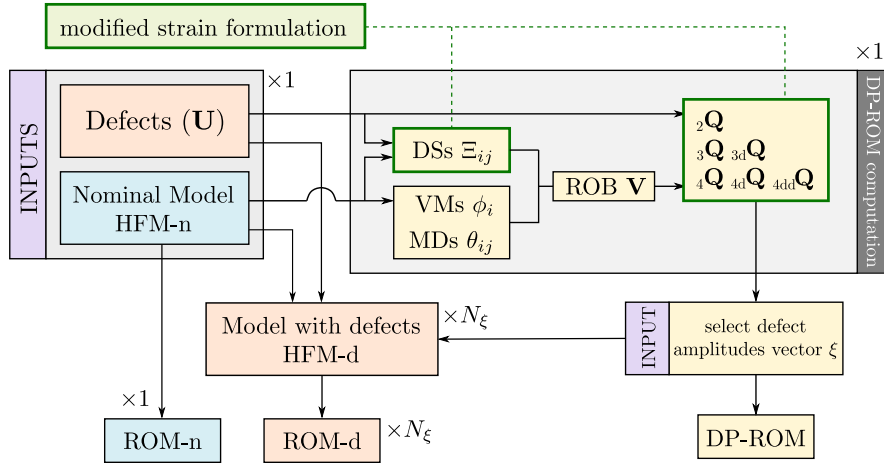
Figure 1: Work-flow map. From the inputs (HFM-n, $\mathbf{U}$ and $\boldsymbol{\xi}$), ROM-n, HFM-d, ROM-d and DP-ROM are computed. Close to each box, it is shown how many times each block must be evaluated (N_ξ is the number of defect combinations). It is also shown (in green) where the modified strain formulation comes into play.

to highlight the fact that defects are significantly changing the response from the nominal case. A summary of the model types is given in Table 2.

5.2. Procedure

Figure 1 synthesizes the sequence of operations followed for the numerical simulations and, at the same time, attempts to put in evidence the contribution of each of the elements individually discussed in the previous sections (as, for instance, the strain formulation and the defects). As common inputs, the user must first specify the nominal geometry and a set of (admissible) displacement fields to model defects (namely,
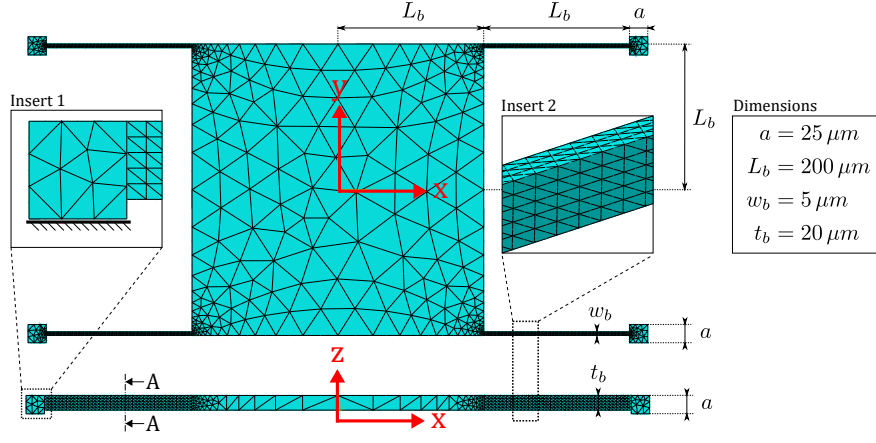
15

Figure 2: MEMS resonator model and mesh, xy-plane view (top) and xz-plane view (bottom). Insert 1 shows an anchor encastered to the ground, while insert 2 is a close-up on the beam's mesh. The structure is meshed in ABAQUS using free quadratic tetrahedra (TET10), counting 17,158 elements, 30,616 nodes and 91,212 dofs.
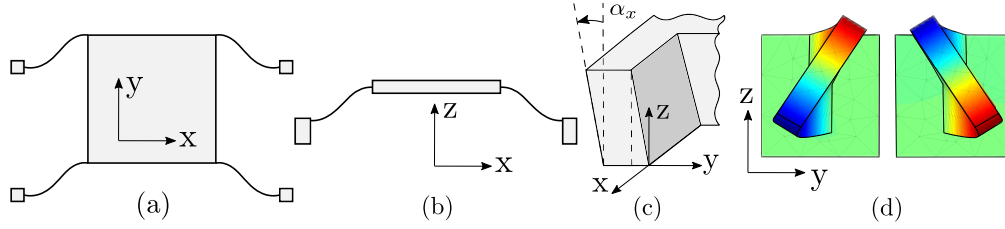

Figure 3: Schematic representation of (a) first vibration mode ϕ_1, (b) second vibration mode ϕ_2, (c) wall angle defect, (d) section A-A of the left beams ($x < 0$, see Fig. 2) at half length for modal derivative θ_{13} (symmetric about y-axis), where the color-map shows y-displacement. For θ_{13} mass does not move, thus is not shown here.

U). ROM-n can be directly computed from HFM-n only. Once the amplitude of the defects (ξ) is defined, HFM-d is instead obtained by shifting HFM-n's node positions by a displacement defined by $\mathbf{d} = \mathbf{U}\xi$. ROM-d follows. Finally, to construct DP-ROM, we compute VMs and MDs using HFM-n (as done for ROM-n) and DSs are obtained using available information about defects. Tensors are then computed exploiting the modified strain formulation. At this point one can select ξ and optionally precompute the quadratic and cubic tensor deviations due to defects (see Section 3.3). Notice that HFM-d and ROM-d have to be computed *for each combination of defects*, while ROM-n (obviously) and DP-ROM are computed *once and for all*, the latter needing just the aforementioned (inexpensive) precomputation. Once the models are ready, time integration is performed in Matlab using Newmark's scheme with full Newton-Raphson iterations. Rayleigh damping is introduced selecting a Q factor of 10,000 in correspondence of the first and second eigenfrequencies. Errors between HFM-d and DP-ROM are then evaluated.
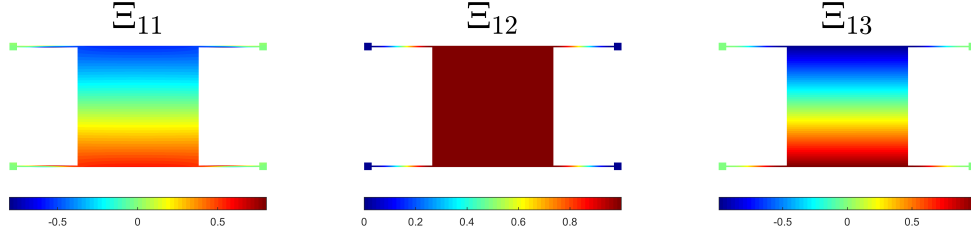
16

Figure 4: Defect Sensitivities for the first VM ϕ_1 with respect to defect $\mathbf{U}_1$, $\mathbf{U}_2$ and $\mathbf{U}_3$. Colormap shows the out-of-plane displacement. Notice that although Ξ_{11} looks very similar to Ξ_{13} if considering the mass only, in the first case the beams undergo torsion, while in the latter pure bending.

6. Numerical tests - I

6.1. Micromechanical resonator FE-model

Description. DP-ROM is tested on a simple MEMS resonator, shown in Fig. 2 (*nominal* structure). Despite not representing any particular real device, such a system is a common element in many MEMS sensors (e.g. accelerometers, gyroscopes), whose dynamic behavior is strongly influenced by the presence of manufacturing defects [52, 53]. The system is composed by a $400 \times 400 \times 20 \, \mu m$ mass suspended by four $200 \times 5 \times 20 \, \mu m$ slender beams, which are connected to the mass at one end and to an anchor at the other end. Anchors are $25 \times 25 \times 25 \, \mu m$ parallelepipeds, encastered at the base, keeping the mass suspended over the ground and free to oscillate. Mesh details are given in Fig. 2 as well. The material is silicon ($E = 148$ GPa, $\rho = 2330 \, \frac{kg}{m^3}$).

Defects. Out of the many possible defects that could be imposed to the structure, we selected three defect shapes that produce, even when small (see below), appreciable differences on the dynamic response with respect to the nominal device. The first shape-defect ($\mathbf{U}_1$) is the second eigenmode ϕ_2, which corresponds to a mass motion along z-axis; the second one ($\mathbf{U}_2$) is given by an inclination of the walls of the structure parallel to the xz-plane by a *wall angle* α_x, that is

$$v_d = \tan(\alpha_x)z, \tag{6.1}$$

being z the elevation of the nodes from ground, and where $u_d = w_d = 0$; the third one ($\mathbf{U}_3$) is the static MD θ_{13}, which basically consists in a counter-torsion of the four beams while the mass stays still. The defect-shapes are shown in Fig. 3. The defect-basis is then

$$\mathbf{U} = [\mathbf{U}_1 \, , \, \mathbf{U}_2 \, , \, \mathbf{U}_3] = [\phi_2 \, , \, \mathbf{U}_{\alpha_x} \, , \, \theta_{13}], \tag{6.2}$$

and the corresponding amplitude vector is

$$\boldsymbol{\xi} = [\xi_1 \, , \, \xi_2 \, , \, \xi_3]^T. \tag{6.3}$$

17

The vectors in $\mathbf{U}$ are normalized such that a value $\xi_i = 1$ corresponds to a maximum displacement of $1\,\mu m$ for $\mathbf{U}_1$ and $\mathbf{U}_3$, and to an angle $\alpha_x = 1°$ for $\mathbf{U}_2$. As it will be shown later, all these defects introduce a coupling between (in-plane) drive and out-of-plane directions.

350

Load case. A nodal mono-harmonic load is placed in the middle of the lateral face of the mass, aligned with y-axis, with frequency equal to the first resonance ω_1 *of the HFM-d*. This is the typical operative condition of a MEMS resonator, which are kept at resonance with a Phase Locked Loop (PLL) and Amplitude Gain Control (AGC). Notice that, for each simulation, the natural frequencies of the system may slightly change depending on the imposed defects: for each set of defects then, the HFM-d's first eigenfrequency is used for HFM-d, ROM-d and DP-ROM (but not for ROM-n, which is always driven at the nominal natural frequency ω_{1n}). Figure 3a schematically shows the actuation mode ϕ_1 (*drive mode*).

Reduction Basis. For every reduced model, the ROB is composed by the first (24.2 kHz)[3], second (79.6 kHz) and third vibration modes (139.5 kHz) with their respective MDs (for a total of 9 vectors). In the case of the DP-ROM, also defect sensitivities are included, for a total of 9 DSs (derivatives of the 3 VMs with respect to each defect-shape). Notice that for the present study we include in the basis even those DSs relative to defects coinciding with VMs (namely, $\mathbf{U}_1$). This is done in order to avoid a special treatment for this case, keeping the analysis as general as possible. Again, hints on how neglecting VM-related DSs would change the analysis are given in Appendix A. Figure 4 shows the DSs related to the drive mode ϕ_1.

6.2. Error evaluation

To assess the accuracy of the method, we adopt the global relative error (GRE) as an error indicator [49], defined as

$$GRE_t = \frac{\sqrt{\sum_{i=1}^{N_t} (\mathbf{p}_i - \hat{\mathbf{p}}_i)^T (\mathbf{p}_i - \hat{\mathbf{p}}_i)}}{\sqrt{\sum_{i=1}^{N_t} \mathbf{p}_i^T \mathbf{p}_i}} \times 100, \qquad (6.4)$$

where $\mathbf{p}_i = \mathbf{p}(t_i)$ is the displacement vector for the i-th time step of the reference solution (HFM-d) and where $\hat{\mathbf{p}}_i$ is the corresponding approximated solution.

Equation (6.4) considers the totality of displacements, disregarding the fact that the order of magnitude of the response along the three directions is different. It is then useful to define the GRE separately for the out-of-plane direction as:

$$GRE_z = \frac{\sqrt{\sum_{i=1}^{N_t} (\mathbf{w}_i - \hat{\mathbf{w}}_i)^T (\mathbf{w}_i - \hat{\mathbf{w}}_i)}}{\sqrt{\sum_{i=1}^{N_t} \mathbf{w}_i^T \mathbf{w}_i}} \times 100, \qquad (6.5)$$
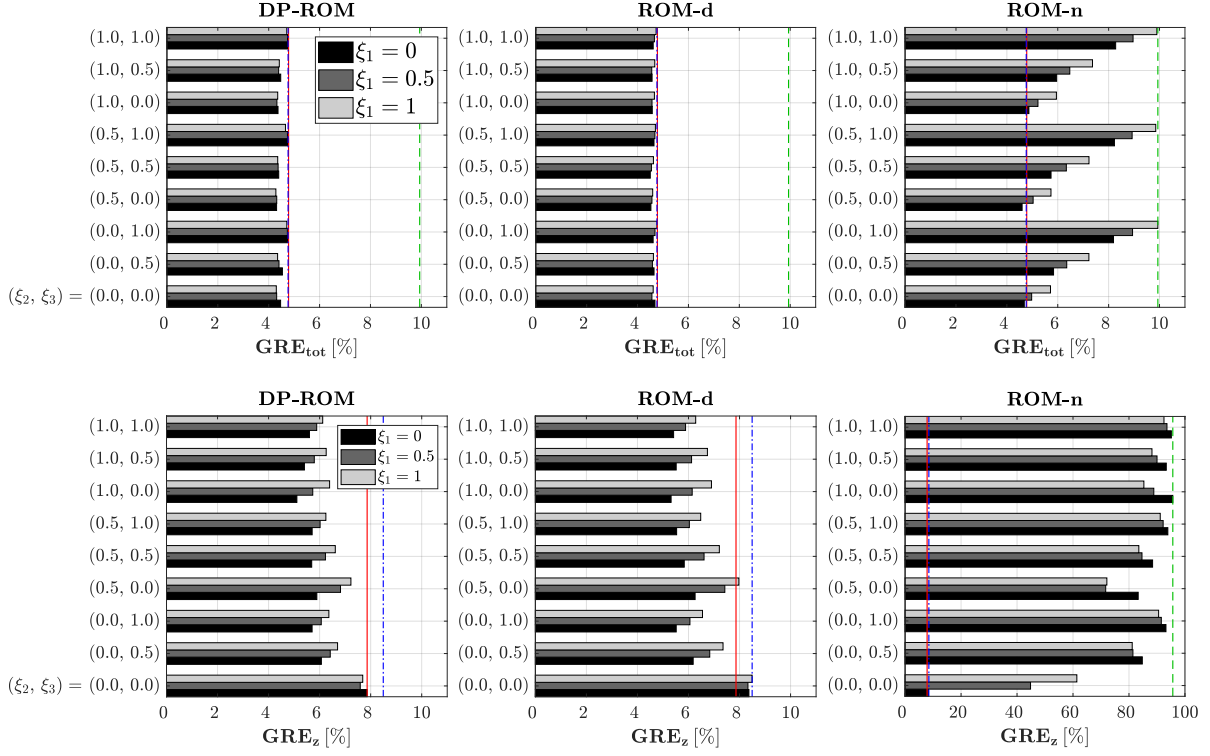
---

[3]Values referred to HFM-n

18

Figure 5: Global Relative Errors (GRE) for the three ROMs. On the vertical axis the pair (ξ_2, ξ_3) is shown. For each pair, the three bars indicate a different value for ξ_1. The vertical lines mark the maximum errors for the DP-ROM (solid, red), ROM-d (dash-dotted, blue) and ROM-n (dashed, green).

where **w** is the z-displacement vector. In many MEMS applications, displacements due to unwanted coupling
between axes (as it is here the case between drive and z-direction) superimpose to a desired measurement sig-
nal. Their correct estimation is therefore critical. Figure 5 shows the errors considering all the displacements
(top) and only **w** (bottom). In both cases, we can see that the ROM-d and DP-ROM yield approximately
the same errors. Instead, looking at the performances of ROM-n, it can be easily seen that along the out-
of-plane direction errors become immediately unacceptable, as the defects lead to a coupling between drive
and z-direction which is not present in the nominal case. It should also be noted that the displacements in z
are much smaller than the ones along y (drive direction), therefore y-errors tend to "hide" z-errors in GRE_t.
Figure 6 shows the time response at the force application node in the three directions in the nominal case and
in the $\xi_1 = \xi_2 = \xi_3 = 1$ case. To validate our in-house Matlab code, results were compared with ABAQUS
ones for the nominal case, showing agreement. Small discrepancies in the x-response are attributed to possi-
ble differences between our Matlab code and ABAQUS in the FE formulation, integration procedures, solvers
and convergence tolerances (notice that due to the symmetry of the nominal problem the displacement u,
which is in the order of 10^{-5}, should be rigorously zero at the forcing location; therefore u can be imputed to
numerical reasons and mesh asymmetries only). Notice that, while the response along z changes significantly
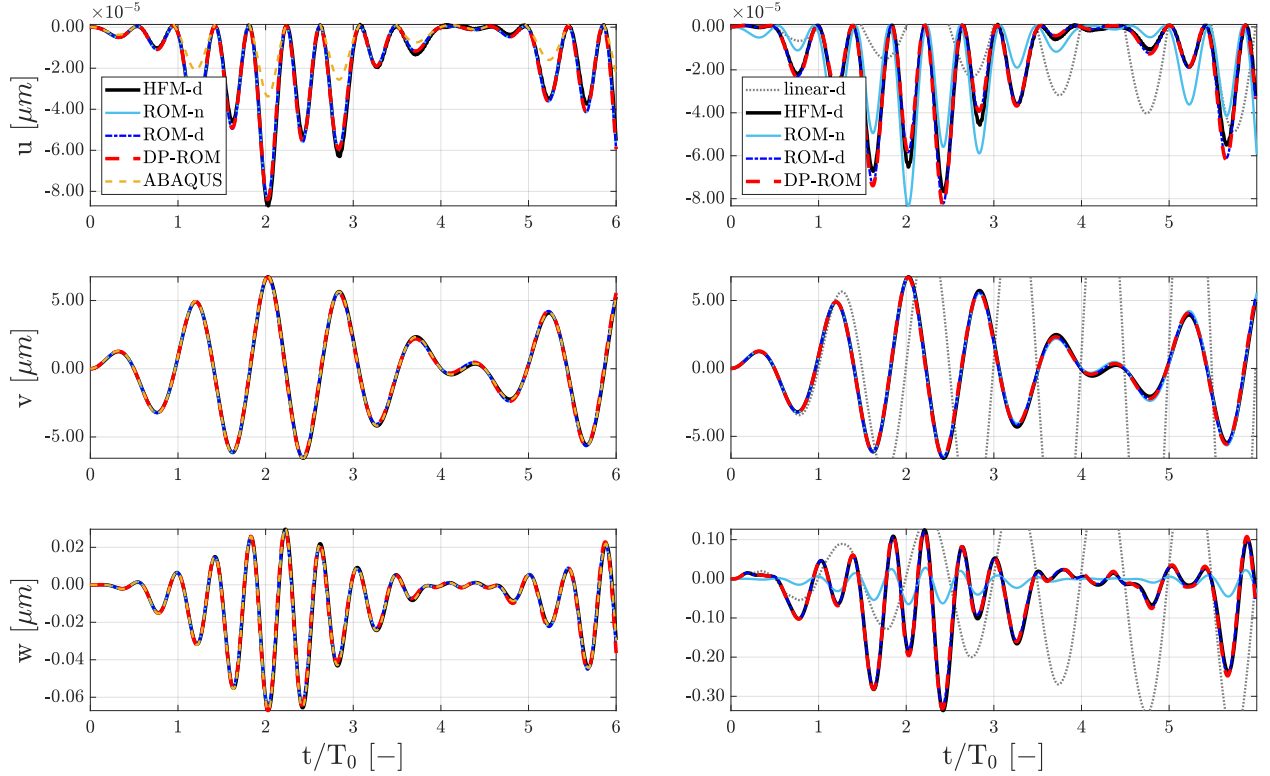
Figure 6: Time domain response at the force application node along the three directions. Left: results for the nominal configuration ($\xi_1 = \xi_2 = \xi_3 = 0$) for all the models plus a full model run on ABAQUS. Right: results for the $\xi_1 = \xi_2 = \xi_3 = 1$ case. T_0 is the period of the harmonic driving force.

from case to case, the x and y responses are barely affected by the presence of the defects.

6.2.1. Role of the reduction basis

We briefly want to stress the importance of using the correct reduction basis. Given the assumption of small defects, one may be driven to think that it might actually be enough to use the *nominal* reduction basis $\mathbf{V}_{nom}$ (i.e. the basis comprising VMs and MDs only, computed on the nominal geometry) not only for ROM-n, but also for ROM-d and DP-ROM. To dispel this doubt and further support the arguments already discussed in Section 4, we ran a numerical test for the MEMS resonator model ($\xi_1 = \xi_2 = \xi_3 = 1$ case) when using the same *nominal* ROB used for ROM-n, that is $\mathbf{V}_{nom} = [\mathbf{\Phi}, \mathbf{\Theta}]$. Again, 3 VMs and their corresponding 6 MDs are included in the basis. Eigenfrequencies, time responses and GREs are shown in Fig. 7. As it can be easily observed, the two ROMs yield now completely different results, with a drastic overestimation of the first eigenfrequency. It is thus evident how information about the defects must be present both in the model to be reduced *and* in the reduction basis itself.

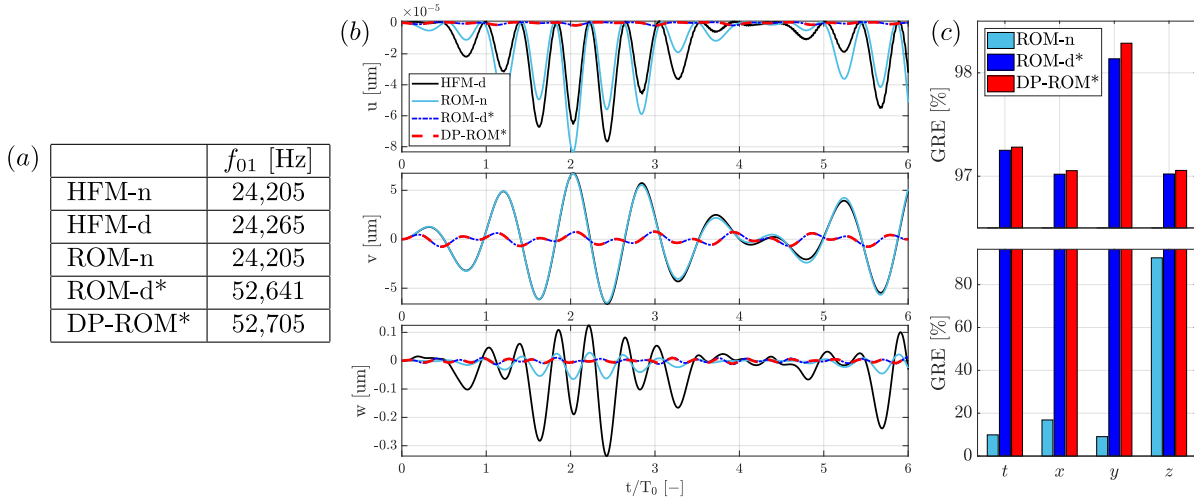**Remark 3** (*ROM-d vs DP-ROM*). Looking at Fig. 7, one can also see that even when using the *same*

20

Figure 7: Simulations for ROM-d and DP-ROM when using the same (nominal) reduction basis as ROM-n. The two model are marked by a * to denote the differences with respect to the definitions given in Table 2. The testing conditions are the same used for Fig. 6 (right). In particular, we have again $\xi_1 = \xi_2 = \xi_3 = 1$. (a) First eigenfrequencies for the different models, (b) time domain responses, (c) errors in terms of GRE (total and for individual axes). Plot is split to increase visibility.

reduction basis, ROM-d and DP-ROM lead to slightly different results (regardless of how wrong they might be with respect to HFM-d). This follows from the fact that ROM-d is computed from HFM-d whereas DP-ROM from HFM-n, with the modified strain formulation to take defects into account. As such, the latter is just an approximation of the former. Small discrepancies are therefore expected. The only case in which ROM-d and DP-ROM would coincide would be the one where $\boldsymbol{\xi} = \mathbf{0}$ *and* $\mathbf{V}_{ROM-d} = \mathbf{V}_{DP-ROM}$. The first condition would make VMs (and MDs) of the nominal and of the defected models coincide, while the second would also imply that DSs are either added to $\mathbf{V}_{ROM-d}$ or removed from $\mathbf{V}_{DP-ROM}$.

6.3. Computational times

In order to assess the computational savings provided by the proposed method, we define three speed-up coefficients as

$$SP1 = \frac{t_{full}}{t_{online}}, \quad SP2 = \frac{t_{full}}{t_{online} + t_{offline}}, \quad SP3 = \frac{t_{full}N_{on}}{t_{online}N_{on} + t_{offline}N_{off}}, \quad (6.6)$$

where t_{full} is the (online) computational time for the full analysis of HFM-d, t_{online} and $t_{offline}$ are the ROMs' online and offline times respectively, N_{on} is the number of online runs and N_{off} is the number of times a ROM has been computed. Notice that $t_{offline}$ accounts for both the times for the ROB and tensors computation.

All the simulations have been carried out on the Euler cluster of ETH Zürich (with 27 CPUs) in Matlab R2017b, using in-house developed codes. This was done mainly in order to make a fair assessment of the approximation errors discussed in the previous section by avoiding unwanted/unforeseen error sources. However, it would be unfair to compute speed-ups referring to the full simulation carried out in this environment,

21

Table 3: Computational times (in seconds) and speed-ups (average values). Speed-ups are computed using ABAQUS' online time (average value over 10 cluster runs) as reference. All the simulations (both on ABAQUS and Matlab) were run on ETH Zürich Euler cluster with 27 CPUs (4GB RAM each). The times marked by * are the ones that are affected by parallel computing. The small difference in ROM-d and DP-ROM online times is due to the number of reduced coordinates (9 and 18, respectively).

	offline (basis)	offline (tensors)	online	N_{off}	N_{on}	total time (27 cases)	total time (hh:mm:ss)	SP1 (online)	SP2 (on+off, 1 case)	SP3 (on+off, 27 cases)
HFM-n (Abaqus)	-	-	2,399.7*	0	27	64,792	17:59:52	-	-	-
ROM-d	18.2	112.1*	5.2	27	27	3,659	1:00:58	461.5	17.7	17.7
DP-ROM	35.9	174.5*	5.8	1	27	367	0:06:07	413.7	11.1	176.5

for it would be much slower with respect to a state-of-art commercial software. For this reason, speed-ups reported in Table 3 are computed with reference to a full (nominal) simulation in ABAQUS/CAE 6.14-1 (same model HFM-n, load and fixed time steps). All computational times are shown in Table 3 as well.

As it can be easily observed, online speed-ups (SP1) are very high, as it is usually the case for all tensorial approaches and other reduction techniques. To make a more comprehensive performance assessment, it is better to look at SP2, which includes the offline costs. It is however to stress the fact that, if the simulation time-span is large enough, $t_{offline}$ may become negligible compared to t_{online} so that $SP2 \rightarrow SP1$ for $t_{online} \rightarrow +\infty$. This holds true for SP3 as well. However, if the same ROM can be exploited more than once, be it for different load cases or for different parameter sets - as in the case of the DP-ROM, we have that $SP3 \rightarrow SP1$ even for $N_{on} \rightarrow +\infty$. In the present case, for a moderately short time-span and relatively low number of simulations, we have $SP3 = 175.5$, almost half of the theoretical maximum limit $SP1 = 413.7$. Following these considerations, we can confidently say that the DP-ROM, if fully exploited as in the intention of the authors, will have $SP3 \approx SP1$. As already stated in the introduction, a Monte-Carlo analysis would make the perfect fit with this method, and one could think to couple it even with uncertainty quantification methods [54].

6.4. About Scalability

Before concluding this section, we would like to make a few comments on how computational times are expected to change with the size of the full model and on the tensors computation.

On the one hand, considering *online* times, it is known that HFM times grow more than linearly with the number of dofs of the structure. In contrast, the original size of the model is irrelevant for ROMs, and online speed is determined by the size of the ROB. Even in this case however, computational times grow more than linearly with the basis size. On the other hand, ROM *offline* costs grow almost *linearly* with the number of elements thanks to element-level projection assembly. Moreover, the number of *dofs of the element* (30 for the 10-nodes tetrahedra TET10 in our test case) greatly affects performances.

Additionally, to give a rough idea of the influence of the basis dimension and of parallel computing,
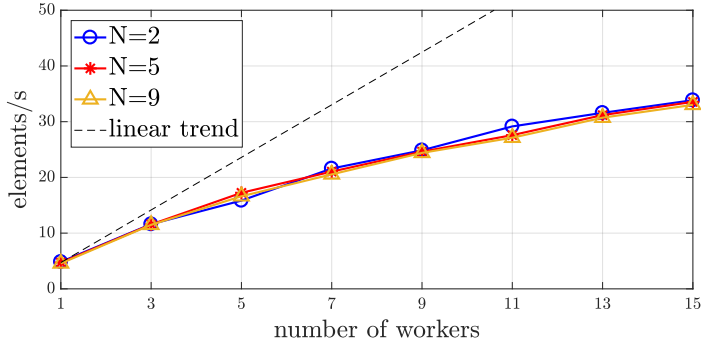
Figure 8: Tensor computational speed as a function of the number of parallel Matlab workers. N is the number of vectors in the reduced order basis. Data are referred to the MEMS model described in this work, notice however that these values remain almost unchanged when coarser or finer meshes were considered.

the tensor computational speed (in terms of elements per second) is shown in Fig. 8. These results were obtained in Matlab R2017a on a local machine equipped with 2 Intel(R) Xeon(R) CPUs (E5-268W 0) @ 3.10 GHz and 64 GB RAM. As it is often the case with parallel computing, speed grows less than linearly with the number of workers. The impact of ROB's size is not negligible, but very weak if compared to other parameters' one. Finally, notice once more that Matlab was used to compute tensors. Thus, a Fortran or C++ dedicated routine could greatly improve performances, reducing offline times and making the method even more attractive.

7. Numerical tests - II

In the previous section, a structure subject to multiple defects was studied with the aim to assess the accuracy and the speed of the proposed method. In that setup the focus was on correctly describing cross-coupling effects. These, however, would likely manifest in a linear setting as well (even if, of course, in a different manner). In this example, instead, we consider the simple case of a beam, clamped at both ends, where the defect will deform the nominal structure into a shallow arch, with the purpose to study a case in which the presence of the defect drastically changes the nonlinear dynamics of the structure. The silicon beam has the same dimension of the suspension beams of the previous test case, with length L_b along x, width w_b along y and thickness t_b along z (see Fig. 2). We used a mesh with 320 hexahedral quadratic elements (HEX20), for a total of 2117 nodes and 6129 dofs. The defect shape is given by

$$v_d(x, \xi) = \xi \cos\left(\frac{\pi}{L_b} x\right), \quad x \in [-L_b/2, \, L_b/2], \tag{7.1}$$

where ξ is the amplitude parameter ($u_d = w_d = 0$). The load, $f_{ext} = step(t)$, is placed at half length on one edge of the beam and is aligned with the positive y-axis. For ROM-n and ROM-d, the reduction basis contains the first 5 VMs and 15 MDs, while for DP-ROM it includes even 5 DSs. Figure 9 shows the errors in the forcing direction and the time responses at the excitation node in the two worst cases. As it can be seen, the GRE is almost always less than 10% and the hardening/softening behavior of the shallow arch is nicely captured by the DP-ROM, even for very large defects ($\xi = \pm 100\% \, w_b$). Higher order harmonics in the full solution, of course, cannot be captured by the tested ROMs due to truncation of the basis. In analogy with
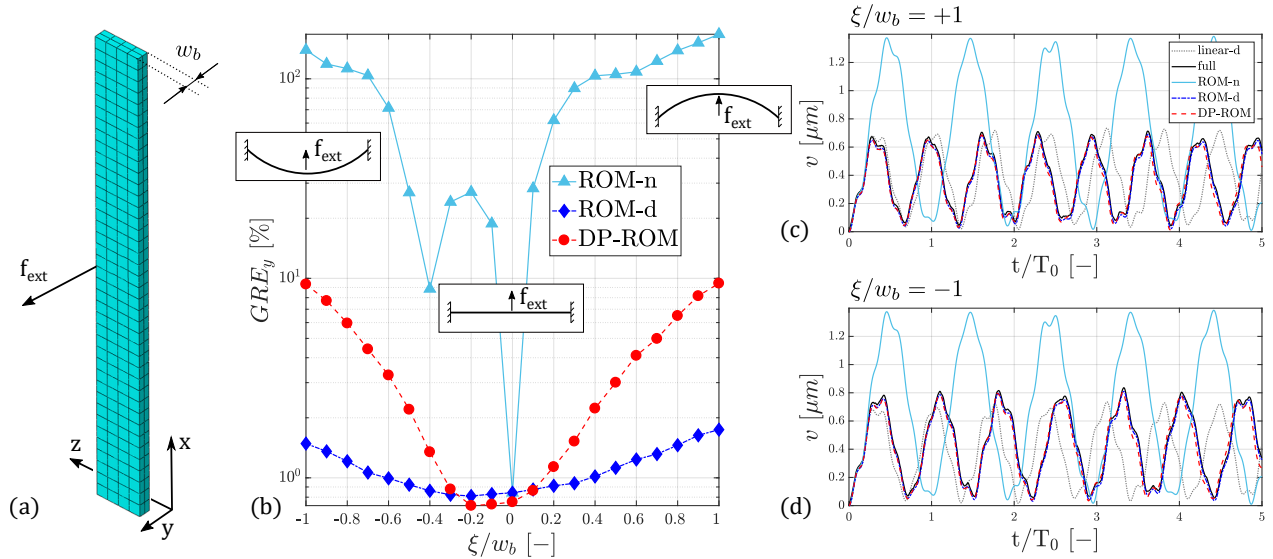
23

Figure 9: Shallow-arch defect. (a) Model mesh, (b) error along y-axis (GRE_y, in logarithmic scale), for $\xi \in [-5, +5]$, step-load time domain responses in y-direction in the *worst cases* for positive (c) and negative (d) values of ξ. T_0 is the period corresponding to the first eigenfrequency of the nominal structure; $w_b = 5\,\mu m$ is the beam thickness in y-direction. HFM-d linear responses (gray dotted lines) are shown in (c) and (d) to put in evidence the hardening/softening behaviors.

what we have done in the previous test case, we reported even the responses and the errors we would obtain if using the nominal model with no defects. Notice that the kink in ROM-n's GRE_y is purely coincidental (for those particular defect amplitudes and load level, the softening behavior of the structure brings the nominal response close to the HFM-d's one).

8. Conclusions

In this work we proposed a parametric ROM to describe shape defects, defined in terms of a shifted nodal position of a tri-dimensional mesh with respect to the nominal geometry. These "defect shapes" are embedded in the strain formulation, which allows for the parametrization of the model. Indeed, using tensorial reduction, we showed how these defect shapes can be directly included in a ROM which can be computed once and for all and which yields accurate results in a neighbourhood of the nominal configuration *for any defect shape*. We also discussed the need to enhance the projection basis with defect sensitivities (DSs), which can be computed using the modified strain formulation. Incidentally, DSs could be of interest even in the context of shape optimization, since they can be analytically derived and do not need remeshing. In contrast to many strategies employed in nonlinear parametric model order reduction, no training of the model is needed, so that the offline costs reduce to the computation of the reduced order tensors only. Two numerical examples were given. First, a MEMS resonator was studied under operative conditions, where the presence of defect shapes introduced a not negligible coupling between axes. Error and computational

24

time analyses showed that consistent speed-ups can be achieved with minimal loss of accuracy. Finally, a shallow-arch micro-beam was studied for different heights of the arch under step loading excitation, showing that the hardening/softening behavior of the structure can be accurately represented. All in all, we think that the proposed method provides a very efficient tool to aid the design phase of structures subject to shape defects, as in the case of MEMS industry.

Appendix A. On MDs and DSs for VM-defects

As it has already been pointed out in Section 4, MD $\boldsymbol{\theta}_{ij}$ can also be interpreted as the sensitivity of the structure with respect to a defect coinciding with vibration mode $\boldsymbol{\phi}_i$. To our purposes, this would suggest that if we were to choose a defect-shape from a set of VMs, no further DS would be needed to enhance the reduction basis, as MDs would replace DSs. However, comparing Eq. (4.8) and Eq. (4.3), it turns out that the two expressions are not equivalent.

Selecting a defect $\mathbf{U} = \boldsymbol{\phi}_j$, we have that $\mathbf{A}_{\mathrm{d}} = \mathbf{A}(\mathbf{G}\mathbf{U}^{el}) = \mathbf{A}(\mathbf{G}\boldsymbol{\phi}_j^{el}) = \mathbf{A}_\phi$. By comparing the two expressions:

$$\left.\frac{\partial \mathbf{K}^{el}(\boldsymbol{\phi}_j^{el}\xi_j)}{\partial \xi_j}\right|_{eq} = \mathbf{G}^T\left(\mathbf{H}^T\mathbf{C}_1\mathbf{A}_{\mathrm{d}} + \mathbf{A}_{\mathrm{d}}^T\mathbf{C}_1\mathbf{H}\right)\mathbf{G} \neq \mathbf{G}^T\left[\mathbf{H}^T\mathbf{C}\mathbf{A}_\phi + 2\mathbf{A}_\phi^T\mathbf{C}\mathbf{H}\right]\mathbf{G} = \left.\frac{\partial \mathbf{K}^{el}(\boldsymbol{\phi}_j^{el}\eta_j)}{\partial \eta_j}\right|_{eq}, \quad (A.1)$$

we notice a difference of a factor 2 for the term $\mathbf{A}^T\mathbf{C}\mathbf{H}$ (integration over volume is implicitly assumed). An inexpensive way to assess the impact of this discrepancy is to look at the evolution of the eigenfrequencies of the reduced system when including only MDs and when including also DSs. Figure A.10 shows the eigenfrequencies trends for the model described in Section 5 when the first VM $\boldsymbol{\phi}_1$ is imposed as a defect. As it can be easily observed, for the second and third modes frequencies tend to diverge if DSs are not included. For the present system and the selected defect amplitudes however the percent error is very small, and one
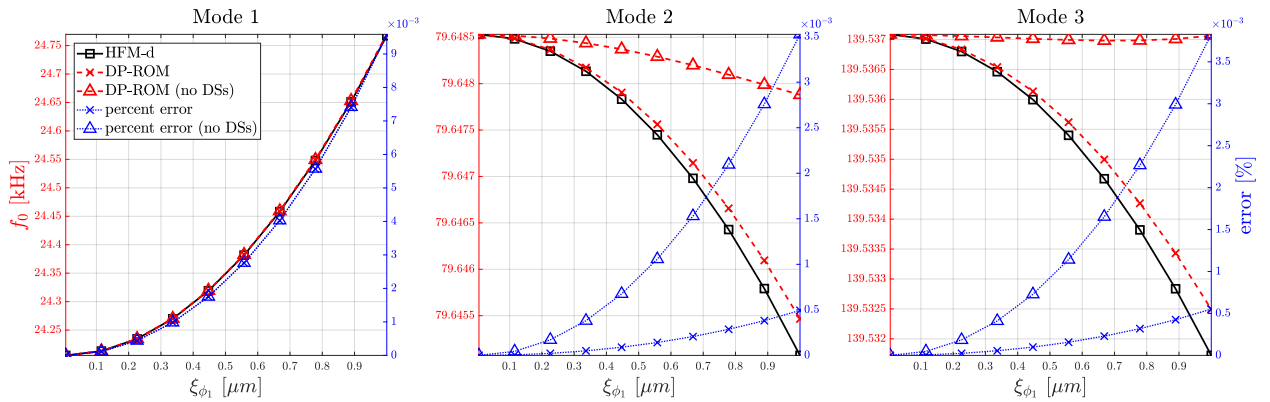

Figure A.10: First three natural frequencies for increasing defect amplitudes. Eigenfrequencies for HFM-d (solid black line), for DP-ROM with and without DSs (red dashed lines) are shown on the left vertical axis. Percent errors (blue, dotted lines) are shown on the right vertical axis. $\boldsymbol{\phi}_1$ is the imposed defect.

25

could then think to use only MDs in the basis. Finally, notice that each defect-shape might have a different impact on the accuracy on the DP-ROM: for instance, imposing the second VM as a defect to our nominal model, we could show that errors are more pronounced on the first eigenfrequency if DSs are not included. For this reason, we recommend to critically choose whether to exclude or not DSs case by case.

References

[1] K.-J. Bathe, Finite Element Procedures, 2014.

[2] R. Craig, M. Bampton, Coupling of Substructures for Dynamic Analyses 6 (1968) 1313–1319.

[3] S. Rubin, Improved Component-Mode Representation for Structural Dynamic Analysis, AIAA Journal 13 (1975) 995–1006.

[4] D. D. Klerk, D. J. Rixen, S. N. Voormeeren, General Framework for Dynamic Substructuring: History, Review and Classification of Techniques, AIAA Journal 46 (2008) 1169–1181.

[5] M. S. Allen, D. Rixen, M. van der Seijs, P. Tiso, T. Abrahamsson, R. L. Mayes, Substructuring in Engineering Dynamics, volume 594 of *CISM International Centre for Mechanical Sciences*, Springer International Publishing, Cham, 2020. URL: http://link.springer.com/10.1007/978-3-030-25532-9. doi:10.1007/978-3-030-25532-9.

[6] M. Balajewicz, D. Amsallem, C. Farhat, Projection-based model reduction for contact problems, International Journal for Numerical Methods in Engineering 106 (2015) 644–663.

[7] M. Géradin, D. J. Rixen, A nodeless' dual superelement formulation for structural and multibody dynamics application to reduction of contact problems, International Journal for Numerical Methods in Engineering 106 (2016) 773–798.

[8] B. Blockmans, T. Tamarozzi, F. Naets, W. Desmet, A nonlinear parametric model reduction method for efficient gear contact simulations, International Journal for Numerical Methods in Engineering 102 (2015) 1162–1191.

[9] F. Pichler, W. Witteveen, P. Fischer, Reduced-Order Modeling of Preloaded Bolted Structures in Multibody Systems by the Use of Trial Vector Derivatives, Journal of Computational and Nonlinear Dynamics 12 (2017) 051032.

[10] L. Wu, P. Tiso, Nonlinear model order reduction for flexible multibody dynamics: a modal derivatives approach, Multibody System Dynamics 36 (2016) 405–425.

[11] L. Wu, P. Tiso, K. Tatsis, E. Chatzi, F. van Keulen, A modal derivatives enhanced Rubin substructuring method for geometrically nonlinear multibody systems, Multibody System Dynamics 45 (2019) 57–85.

[12] R. J. Kuether, B. J. Deaner, J. J. Hollkamp, M. S. Allen, Evaluation of geometrically nonlinear reduced-order models with nonlinear normal modes, AIAA Journal 52 (2015) 3273–3285.

[13] J. J. Hollkamp, R. W. Gordon, Reduced-order models for nonlinear response prediction: Implicit condensation and expansion, Journal of Sound and Vibration 318 (2008) 1139–1153.

[14] C. Touzé, M. Vidrascu, D. Chapelle, Direct finite element computation of non-linear modal coupling coefficients for reduced-order shell models, Computational Mechanics 54 (2014) 567–580.

[15] S. Jain, P. Tiso, Simulation-free hyper-reduction for geometrically nonlinear structural dynamics: A quadratic manifold lifting approach, Journal of Computational and Nonlinear Dynamics 13 (2018) 1–12.

[16] D. Ryckelynck, A priori hyperreduction method: an adaptive approach, Journal of Computational Physics 202 (2005) 346–366.

[17] A. K. Noor, J. M. Peterst, Reduced Basis Technique for Nonlinear Analysis of Structures, AIAA Journal 18 (1980) 455–462.

[18] M. P. Mignolet, A. Przekop, S. A. Rizzi, S. M. Spottswood, A review of indirect/non-intrusive reduced order modeling of nonlinear geometric structures, Journal of Sound and Vibration 332 (2013) 2437–2460.

[19] M. Amabili, Reduced-order models for nonlinear vibrations, based on natural modes: the case of the circular cylindrical shell, Philosophical Transactions of the Royal Society A: Mathematical, Physical and Engineering Sciences 371 (2013) 20120474.

[20] S. R. Idelsohn, A. Cardona, A reduction method for nonlinear structural dynamic analysis, Computer Methods in Applied Mechanics and Engineering 49 (1985) 253–279.

[21] C. S. Sombroek, P. Tiso, L. Renson, G. Kerschen, Numerical computation of nonlinear normal modes in a modal derivative subspace, Computers and Structures 195 (2018) 34–46.

[22] C. Acar, A. Shkel, MEMS Vibratory Gyroscopes, Springer, 2008.

[23] H. Farokhi, M. H. Ghayesh, M. Amabili, Nonlinear dynamics of a geometrically imperfect microbeam based on the modified couple stress theory, International Journal of Engineering Science 68 (2013) 11–23.

[24] P. Kołakowski, M. Wikło, J. Holnicki-Szulc, The virtual distortion method - A versatile reanalysis tool for structures and systems, Structural and Multidisciplinary Optimization 36 (2008) 217–234.

[25] U. Kirsch, M. Bogomolni, I. Sheinman, Nonlinear dynamic reanalysis of structures by combined approximations, Computer Methods in Applied Mechanics and Engineering 195 (2006) 4420–4432.

[26] U. Kirsch, A unified reanalysis approach for structural analysis, design, and optimization, Structural and Multidisciplinary Optimization 25 (2003) 67–85.

[27] M. Zeoli, F. van Keulen, M. Langelaar, Fast reanalysis of geometrically nonlinear problems after shape modifications, in: 6th World Congresses of Structural and Multidisciplinary Optimization, June, Rio de Janeiro, 2005, pp. 1–11.

[28] L. Daniel, O. C. Siong, L. S. Chay, A Multiparameter Moment Matching Model Reduction Approach for Generating Geometrically Parameterized Interconnect Performance Models, Tcad 23 (2004) 1–15.

[29] B. Fröhlich, J. Gade, F. Geiger, M. Bischoff, P. Eberhard, Geometric element parameterization and parametric model order reduction in finite element based shape optimization, Computational Mechanics (2018).

[30] S. van Ophem, E. Deckers, W. Desmet, Parametric model order reduction without a priori sampling for low rank changes in vibro-acoustic systems, Mechanical Systems and Signal Processing 130 (2019) 597–609.

[31] P. Benner, S. Gugercin, K. Willcox, A Survey of Projection-Based Model Reduction Methods for Parametric Dynamical Systems, SIAM Review 57 (2015) 483–531.

[32] D. Xiao, F. Fang, A. G. Buchan, C. C. Pain, I. M. Navon, A. Muggeridge, Non-intrusive reduced order modelling of the Navier-Stokes equations, Computer Methods in Applied Mechanics and Engineering 293 (2015) 522–541.

[33] D. Xiao, F. Fang, C. C. Pain, I. M. Navon, A parameterized non-intrusive reduced order model and error analysis for general time-dependent nonlinear partial differential equations and its applications, Computer Methods in Applied Mechanics and Engineering 317 (2017) 868–889.

[34] J. S. Hesthaven, S. Ubbiali, Non-intrusive reduced order modeling of nonlinear problems using neural networks, Journal of Computational Physics 363 (2018) 55–78.

[35] M. Oulghelou, C. Allery, Non intrusive method for parametric model order reduction using a bi-calibrated interpolation on the Grassmann manifold (2018) 1–25.

[36] R. Zimmermann, Manifold interpolation and model reduction (2019) 1–36.

[37] Y. Le Guennec, J. P. Brunet, F. Z. Daim, M. Chau, Y. Tourbier, A parametric and non-intrusive reduced order model of car crash simulation, Computer Methods in Applied Mechanics and Engineering 338 (2018) 186–207.

[38] X. Q. Wang, G. P. Phlipot, R. A. Perez, M. P. Mignolet, Locally enhanced reduced order modeling for the nonlinear geometric response of structures with defects, International Journal of Non-Linear Mechanics 101 (2018) 1–7.

[39] X. Q. Wang, P. J. O'Hara, M. P. Mignolet, J. J. Hollkamp, Reduced Order Modeling with Local Enrichment for the Nonlinear Geometric Response of a Cracked Panel, AIAA Journal 57 (2018) 421–436.

[40] B. Budiansky, Dynamic Buckling of Elastic Structures: Criteria and Estimates, in: Proceedings of an International Conference Held at Northwestern University, Evanston, Illinois, Pergamon Press Ltd, 1967. URL: `http://linkinghub.elsevier.com/retrieve/pii/B9781483198217500107`. doi:10.1016/B978-1-4831-9821-7.50010-7.

[41] W. T. Koiter, Elastic Stability, Buckling and Post-Buckling Behaviour, in: Proceedings of the IU-TAM Symposium on Finite Elasticity, Springer Netherlands, 1981, pp. 13–24. URL: `http://www.springerlink.com/index/10.1007/978-94-009-7538-5{_}2`. doi:10.1007/978-94-009-7538-5_2.

[42] J. Wedel-Heinen, Vibration of geometrically imperfect beam and shell structures, International Journal of Solids and Structures 27 (1991) 29–47.

[43] E. L. Jansen, A perturbation method for nonlinear vibrations of imperfect structures: Application to cylindrical shell vibrations, International Journal of Solids and Structures 45 (2008) 1124–1145.

[44] P. Tiso, Finite element based reduction methods for static and dynamic analysis of thin-walled structures, Ph.D. thesis, Technische Universiteit Delft, 2006.

[45] T. Lassila, G. Rozza, Parametric free-form shape design with PDE models and reduced basis method, Computer Methods in Applied Mechanics and Engineering 199 (2010) 1583–1592.

[46] M. A. Crisfield, Non-linear Finite Element Analysis of Solids and Structures, Volume 1, volume 1, 1991. URL: `http://eu.wiley.com/WileyCDA/WileyTitle/productCd-0470666447.html`. doi:10.1017/CBO9781107415324.004. arXiv:arXiv:1011.1669v3.

[47] S. Jain, Model Order Reduction for Non-linear Structural Dynamics, 2015. URL: `https://repository.tudelft.nl/islandora/object/uuid{%}3Acb1d7058-2cfa-439a-bb2f-22a6b0e5bb2a`. doi:uuid:cb1d7058-2cfa-439a-bb2f-22a6b0e5bb2a.

[48] B. W. Bader, T. G. Kolda, et al., Matlab tensor toolbox version 3.0-dev, Available online, 2017. URL: `https://www.tensortoolbox.org`.

[49] S. Jain, P. Tiso, J. B. Rutzmoser, D. J. Rixen, A quadratic manifold for model order reduction of nonlinear structural dynamics, Computers and Structures 188 (2017) 80–94.

[50] A. Hay, J. Borggaard, I. Akhtar, D. Pelletier, Reduced-order models for parameter dependent geometries based on shape sensitivity analysis, Journal of Computational Physics 229 (2010) 1327–1352.

29

[51] P. Tiso, Optimal second order reduction basis selection for nonlinear transient analysis, in: Proceedings of the 29th IMAC A Conference on Structural Dynamics 2011, volume 3, 2011, pp. 27–39. URL: `http://link.springer.com/10.1007/978-1-4419-9299-4http://link.springer.com/10.1007/978-1-4419-9299-4{_}3`. doi:10.1007/978-1-4419-9299-4_3.

[52] M. S. Weinberg, A. Kourepenis, Error sources in in-plane silicon tuning-fork MEMS gyroscopes, Journal of Microelectromechanical Systems 15 (2006) 479–491.

[53] M. Izadi, F. Braghin, D. Giannini, D. Milani, F. Resta, M. F. Brunetto, L. G. Falorni, G. Gattere, L. Guerinoni, C. Valzasina, A comprehensive model of beams' anisoelasticity in MEMS gyroscopes, with focus on the effect of axial non-vertical etching, 5th IEEE International Symposium on Inertial Sensors and Systems, INERTIAL 2018 - Proceedings (2018) 1–4.

[54] S. P. Pivovarov D, Willner K, Challenges of order reduction techniques for problems involving polymorphic uncertainty, GAMM-Mitteilungen (2019).